TKK Dissertations 148
Espoo 2008

MULTISCALE MODELING OF EFFECTS DUE TO IMPURITY CLUSTERING IN SEMICONDUCTOR SYSTEMS

Doctoral Dissertation

Teemu Hynninen

Helsinki University of Technology
Faculty of Information and Natural Sciences
Department of Applied Physics

TKK Dissertations 148
Espoo 2008

MULTISCALE MODELING OF EFFECTS DUE TO IMPURITY CLUSTERING IN SEMICONDUCTOR SYSTEMS

Doctoral Dissertation

Teemu Hynninen

Dissertation for the degree of Doctor of Science in Technology to be presented with due permission of the Faculty of Information and Natural Sciences for public examination and debate in Auditorium K at Helsinki University of Technology (Espoo, Finland) on the 19th of December, 2008, at 13 o'clock.

Helsinki University of Technology
Faculty of Information and Natural Sciences
Department of Applied Physics

Teknillinen korkeakoulu
Informaatio- ja luonnontieteiden tiedekunta
Teknillisen fysiikan laitos

Distribution:
Helsinki University of Technology
Faculty of Information and Natural Sciences
Department of Applied Physics
P.O. Box 1100
FI - 02015 TKK
FINLAND
URL: http://tfy.tkk.fi/
Tel. +358-9-451 3111
Fax +358-9-451 3116
E-mail: teemu.hynninen@tkk.fi

© 2008 Teemu Hynninen

ISBN 978-951-22-9681-1
ISBN 978-951-22-9682-8 (PDF)
ISSN 1795-2239
ISSN 1795-4584 (PDF)
URL: http://lib.tkk.fi/Diss/2008/isbn9789512296828/

TKK-DISS-2544

Picaset Oy
Helsinki 2008

ABSTRACT OF DOCTORAL DISSERTATION	HELSINKI UNIVERSITY OF TECHNOLOGY P. O. BOX 1000, FI-02015 TKK http://www.tkk.fi

Author Teemu Hynninen

Name of the dissertation
Multiscale modeling of effects due to impurity clustering in semiconductor systems

Manuscript submitted 07.10.2008	Manuscript revised 17.11.2008
Date of the defence 19.12.2008 at 13 o'clock, TKK main building, auditorium K	
☐ Monograph	☒ Article dissertation (summary + original articles)

Faculty	Faculty of Information and Natural Sciences
Department	Department of Applied Physics
Field of research	Computational materials physics
Opponent(s)	Prof. Graeme Henkelman
Supervisor	Prof. Juhani von Boehm (to 30.06.2008), Prof. Tapio Ala-Nissilä
Instructor	Dr. Adam Foster, Prof. Juhani von Boehm

Abstract

The properties of materials visible to us at the macroscopic scale are due to the microscopic behavior of the atoms in the material. In many cases, small disturbances from an ideal microstructure can lead to completely different behavior at the macroscale. In order to exploit or prevent such phenomena, it is important to understand both the microscopic interactions governing the individual atoms and the mechanisms which lead to the observed collective behavior of the particles at the macroscale. Computational methods can offer insight to such problems, since in a computational scheme it is possible to manipulate the systems at will and without unwanted disturbances. On the other hand, these methods necessarily contain approximations and care must be taken in choosing and combining the methods used for examining the different physically relevant length and time scales.

This dissertation presents computational simulations of the role of impurities and impurity clusters in two types of semiconductor systems. The influence of the microstructure of Mn dopants in the diluted magnetic semiconductors (Ga,Mn)N and (Ga,Mn)As is examined. Also, the effect of metal impurities, such as Cu and Pb, on the surface morphologies of wet etched Si surfaces is studied. In both cases, density-functional calculations are used for studying the microscopic interactions and models based on Monte Carlo schemes are developed for simulating the macroscopic behavior. In the presented work, a direct correspondence between the microstructures of the magnetic semiconductors and their magnetic properties is found, explaining the experimentally observed variations in Curie temperatures. The dependence of the roughness of etched surfaces on the types of impurities present during etching is also explained by different adsorption and cluster formation tendencies of the various impurities on the Si surface.

Keywords	impurities, clusters, magnetic semiconductors, Curie temperature, etching, surface morphology		
ISBN (printed)	978-951-22-9681-1	ISSN (printed)	1795-2239
ISBN (pdf)	978-951-22-9682-8	ISSN (pdf)	1795-4584
Language	English	Number of pages	62 p. + app. 79 p.
Publisher	Department of Applied Physics, Helsinki University of Technology		
Print distribution	Department of Applied Physics, Helsinki University of Technology		

☒ The dissertation can be read at http://lib.tkk.fi/Diss/2008/isbn9789512296828/

VÄITÖSKIRJAN TIIVISTELMÄ	TEKNILLINEN KORKEAKOULU PL 1000, 02015 TKK http://www.tkk.fi

Tekijä Teemu Hynninen

Väitöskirjan nimi

Epäpuhtausklusterien muodostumisen vaikutusten moniskaalamallintaminen puolijohteissa

Käsikirjoituksen päivämäärä	07.10.2008	Korjatun käsikirjoituksen päivämäärä	17.11.2008

Väitöstilaisuuden ajankohta 19.12.2008 klo 13, Teknillisen korkeakoulun päärakennus, luentosali K

☐ Monografia ☒ Yhdistelmäväitöskirja (yhteenveto + erillisartikkelit)

Tiedekunta	Informaatio- ja luonnontieteiden tiedekunta
Laitos	Teknillisen fysiikan laitos
Tutkimusala	Laskennallinen materiaalifysiikka
Vastaväittäjä(t)	Prof. Graeme Henkelman
Työn valvoja	Prof. Juhani von Boehm (30.06.2008 asti), Prof. Tapio Ala-Nissilä
Työn ohjaaja	Dr. Adam Foster, Prof. Juhani von Boehm

Tiivistelmä

Materiaalien makroskooppiset ominaisuudet ovat seurausta niiden atomien käyttäytymisestä mikroskooppisessa mittakaavassa. Monesti pienetkin muutokset mikrorakenteessa voivat johtaa täysin erilaisiin ominaisuuksiin suuremmassa mittakaavassa. Jotta tällaisia ilmiöitä voitaisiin hyödyntää tai tarvittaessa estää, on tunnettava sekä yksittäisiä atomeja ohjaavat mirkoskooppiset vuorovaikutukset että näistä makroskooppisiin ominaisuuksiin johtavat mekanismit. Laskennalliset menetelmät ovat käyttökelpoisia tällaisten ongelmien tutkimisessa, sillä niiden avulla voidaan manipuolida tutkittavia systeemejä täsmälleen halutuilla tavoilla. Toisaalta laskennallisissa malleissa on aina turvauduttava myös approksimaatioihin, joten eri pituus- ja aikamittakaavojen tutkimisessa käytettävät menetelmät on syytä valita huolella eikä niiden yhdistäminen ole aina yksinkertaista.

Tässä väitöskirjassa tarkastellaan laskennallisten simulaatioiden keinoin epäpuhtauksien ja epäpuhtausklusterien vaikutusta kahdessa eri puolijohdesysteemissä. Työssä on tutkittu mangaaniatomien muodostamien rakenteiden merkitystä magneettisten puolijohdemateriaalien (Ga,Mn)N ja (Ga,Mn)As ominaisuuksille sekä metalliepäpuhtauksien kuten kuparin ja lyijyn vaikutusta märkäetsattujen piipintojen pintamorfologiaan. Molemmissa systeemeissä mikroskooppisten vuorovaikutusten voimakkuuksia on laskettu käyttäen tiheysfunktionaaliteoriaa. Makroskooppiset simulaatiot on toteutettu kehittämällä Monte Carlo -menetelmiin perustuvat simulaatiomallit. Väitöstyössä osoitetaan riippuvuus tutkittujen magneettisten puolijohteiden mikrorakenteen sekä niiden magneettisten ominaisuuksien välillä, mikä selittää kokeellisesti havaittua vaihtelua aineiden Curie-lämpötiloissa. Piin etsauksessa metalliepäpuhtauksien tuottamien erilaisten pinnanmuotojen osoitetaan olevan seurausta metallien erilaisista kyvyistä adsorboitua piipinnalle ja muodostaa siellä klustereita.

Asiasanat epäpuhtaudet, klusterit, magneettiset puolijohteet, Curie-lämpötila, etsaus, pintamorfologia

ISBN (painettu)	978-951-22-9681-1	ISSN (painettu)	1795-2239
ISBN (pdf)	978-951-22-9682-8	ISSN (pdf)	1795-4584
Kieli	englanti	Sivumäärä	62 s. + liitteet 79 s.

Julkaisija Teknillisen fysiikan laitos, Teknillinen korkeakoulu

Painetun väitöskirjan jakelu Teknillisen fysiikan laitos, Teknillinen korkeakoulu

☒ Luettavissa verkossa osoitteessa http://lib.tkk.fi/Diss/2008/isbn9789512296828/

Preface

This thesis has been prepared in the Computational Nanoscience group (COMP), in the Department of Applied Physics, Helsinki University of Technology, during 2005-2008.

I thank my instructors and supervisors Dr. Adam Foster, Dr. Hannes Raebiger, Prof. Juhani von Boehm, Prof. Tapio Ala-Nissilä and Acad. Prof. Risto Nieminen for all the support, advice, ideas, practical help and good times they have provided. I am especially grateful to Dr. Miguel Gosálvez, whose aid was indispensable. I would also like to thank all the collaborators and colleagues at COMP and Nagoya University for making this work possible.

This research has been supported by the Academy of Finland through the Centre of Excellence Program (2000-2005 and 2006-2011), project SA 122603 “Role of metal impurities and etchant cations during anisotropic etching” and the JSPS-AKA Bilateral Program with the Academy of Finland. I have been personally supported by a grant from the Finnish Cultural Foundation. The computational resources for this work have been mostly provided by the IT center for science, CSC. This support is gratefully acknowledged.

Family, friends and especially Anu, thank you!

Espoo, November 2008

Teemu Hynninen

Contents

Abstract iii
Tiivistelmä v
Preface vii
Contents ix
List of publications x

Background

1 Introduction 1

2 Studied physical systems 3
2.1 Diluted magnetic semiconductors 3
2.2 Anisotropic wet chemical etching of silicon 5

Methods

3 Calculations at the atomic scale 8
3.1 Density-functional theory 8
3.2 Implementations of the theory 10

4 Simulating macroscopic phenomena 15
4.1 Equilibrium Monte Carlo 15
4.2 Kinetic Monte Carlo 20

Results

5 Microscopic interactions and formation of clusters 24
5.1 Structure and magnetism of Mn clusters 24
5.2 Metal impurities on the H-terminated Si surface 28

6 Macroscale effects of impurities and clusters 33
6.1 Effect of Mn microstructure on Curie temperature 33
6.2 Influence of impurities on surface morphology 36

Conclusions

7 Conclusions 39

References 42

List of publications

This thesis consists of an overview and the following publications:

I T. Hynninen, H. Raebiger, J. von Boehm and Andrés Ayuela, *High Curie temperatures in (Ga,Mn)N from Mn clustering*, Applied Physics Letters **88**, 122501 (2006). © American Institute of Physics 2006

II T. Hynninen, H. Raebiger and J. von Boehm, *A multiscale study of ferromagnetism in clustered (Ga,Mn)N*, Journal of Physics: Condensed Matter **18**, 1561 (2006). © Institute of Physics and IOPP 2006

III T. Hynninen, H. Raebiger and J. von Boehm, *Structural and magnetic properties of (Ga,Mn)N from first principles*, Physical Review B **75**, 125208 (2007). © American Physical Society 2007

IV T. Hynninen, M. Ganchenkova, H. Raebiger and J. von Boehm, *Ferromagnetism and its evolution during long-term annealing in (Ga,Mn)As*, Physical Review B **74**, 195337 (2006). © American Physical Society 2006

V A. S. Foster, M. A. Gosálvez, T. Hynninen, R. M. Nieminen and K. Sato, *First-principles calculations of Cu adsorption on an H-terminated Si surface*, Physical Review B **76**, 075315 (2007). © American Physical Society 2007

VI T. Hynninen, M. A. Gosálvez, A. S. Foster, H. Tanaka, K. Sato, M. Uwaha and R. M. Nieminen, *Effect of Cu impurities on wet etching of Si(110): formation of trapezoidal hillocks*, New Journal of Physics **10**, 013033 (2008). © Institute of Physics and IOPP 2008

VII T. Hynninen, A. S. Foster, M. A. Gosálvez, K. Sato and R. M. Nieminen, *Adsorption of metal impurities on H-terminated Si surfaces and their influence on the wet chemical etching of Si*, Journal of Physics: Condensed Matter **20**, 485005 (2008). © Institute of Physics and IOPP 2008

The author has had an active role in all phases of the research reported in this thesis. He has developed and implemented the magnetic Monte Carlo method used in Publications **II**–**IV** and the impurity part of the kinetic Monte Carlo method used in Publications **VI** and **VII**. The author has performed all the calculations in

Publications **I**, **II**, **III** and **VI**, the Curie temperature calculations in Publication **IV**, a part of the adsorption energy and electron structure calculations in Publication **V**, most of the electronic calculations in Publication **VII**, and all of the kinetic Monte Carlo calculations in Publication **VII**. He has written completely Publications **III**, **VI** and **VII**, and partly Publications **I**, **II**, **IV** and **V**. During the work described in this thesis, the author has also contributed to additional related articles [1–3], not included in the thesis.

1 Introduction

While analytical models can be very good in describing general properties of physical systems, purely theoretical analysis is often impossible when the complexity of the studied phenomena increases. However, many times the most interesting properties of systems are caused by deviations from the ideal, such as defects, dopants, active groups or impurities. Computational methods are often well suited for studying such phenomena, although, such complex systems usually remain very challenging to analyze. First of all, in order to understand the basic rules by which a system operates, one must know the properties of individual defects as well as how they interact. Furthermore, in order to understand the phenomena they induce, one must analyze how the microscopic properties translate to the macroscopic scale. In this thesis, the effects of impurities in two different kinds of physical systems are studied both on the atomistic and the macroscopic level using multiscale modeling methods.

Firstly, the dependence of magnetic properties of the (Ga,Mn)N and (Ga,Mn)As materials on the structures formed by substitutional Mn_{Ga} atoms is analyzed. These compounds belong to a novel group of materials called diluted magnetic semiconductors (DMS's) in which magnetic and semiconducting properties are combined by doping ordinary semiconductor materials with magnetic impurities [4]. Since these materials combine electronic and magnetic degrees of freedom, they have great potential in spin electronics, or spintronics, applications. The goals in spintronics include integrating magnetism based memory applications with electronics-based processing into single devices, improving the efficiency of electronics by using spin in addition to (or instead of) charge to process information, and even creating completely new devices [5–7]. DMS's are especially interesting spintronics materials because, being based on common semiconductor materials such as GaAs and GaN, they could in principle be easily integrated with existing semiconductor technology. So far, one of the main difficulties concerning the use of DMS's in real devices has been the issue of the known DMS materials exhibiting magnetic properties usually only at very low temperatures [8]. To help understand the mechanisms behind the magnetic properties in DMS's, a spin model incorporating clusters of magnetic elements is introduced in this thesis and a connection between the microscopic structures of the magnetic impurities and the magnetic phase transition temperatures of the macroscopic materials is demonstrated.

Secondly, the effect of metal impurities, especially that of Cu and Pb, and impurity clusters on the morphology of Si surfaces during anisotropic wet chemical etching is studied. Silicon is still the most important semiconductor material used in both integrated circuits (IC) and microelectromechanical systems (MEMS), and anisotropic wet chemical etching alone or combined with other fabrication techniques is widely used in IC and MEMS manufacturing [9–12]. The devices made by etching include cantilevers [13], microfluidic systems [14], microneedles [15], inertial sensors [16] and membranes [17], to name a few. The size of the structures fabricated by etching is approaching the nanoscale and this must be matched by the precision of the applied micromachining methods. However, various rough surface morphologies can be observed on etched surfaces, depending on the crystallographic surface orientation and etching conditions [18], which may be detrimental to device performance. The development of rough surfaces is due to a complicated interplay between the silicon surface, the etchant solution and possibly also impurities, making their theoretical and computational analysis challenging. To address the issue of rough surfaces, a kinetic etching simulation method incorporating also etchant impurities has been developed in this thesis. A picture of the role of metal impurities in the surface roughening processes on Si (110) and (100) surfaces is obtained, showing how the formation of impurity clusters can lead to the appearance of etch hillocks.

This overview is organized as follows. The studied physical systems and the central physical phenomena are introduced in Section 2. In Section 3, the quantum mechanical first principles calculations methods used for studying the systems at the atomistic level are presented. Similarly, Section 4 discusses the Monte Carlo techniques applied for simulating the macroscopic behavior of the systems. The results are summarized in Sections 5 and 6 for the first principles calculations of microscopic interactions and the macroscopic simulations, respectively. Finally, Section 7 summarizes and concludes the thesis.

2 Studied physical systems

2.1 Diluted magnetic semiconductors

Along with charge and mass, electrons have a third fundamental property called spin. The spin is a quantum mechanical entity which roughly speaking makes the electron act like a small bar magnet. Modern electronics are mostly based on observing and manipulating electrons using their charge, but the electronic operations could also be based on the spins of electrons. Since electronics are built on semiconductors, a natural raw material for realizing such spintronics would be a semiconductor where the spins can be controlled — a magnetic semiconductor.

Magnetic semiconductors such as Eu chalcogenides were studied already in the 1960's, but these materials are extremely difficult to grow [19]. However, just as common semiconductors can be doped with donor or acceptor impurities to be n- or p-type, they can also be doped with magnetic atoms to produce so-called diluted magnetic semiconductors, as schematically shown in Figure 2.1. These materials can exhibit half-metallic properties, where electrons with spins pointing in one direction partially fill the conduction band and can conduct electricity, like in a metal, while for the electrons with oppositely oriented spins there is a band gap at the Fermi level and the electrons behave as in a semiconductor [20]. Such a property would be ideal for, e.g., creating spin-polarized currents in spintronics applications. While spin-polarization can be achieved with normal magnetic metals as well, it is not easy to integrate them to semiconductor devices. [4]

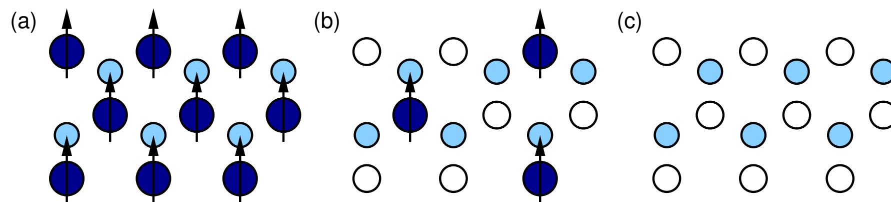

Figure 2.1: (a) A magnetic semiconductor with a regular array of magnetic elements. (b) A diluted magnetic semiconductor where some of the atoms in the host semiconductor have been replaced by magnetic elements. (c) An ordinary non-magnetic semiconductor. The arrows represent magnetic moments, spins.

Having magnetic elements in a material is not enough to make it a magnet. The local magnetic moments, or spins, of the impurities are directed (shown as arrows

in Figure 2.1) and if the spins point in opposite directions, the magnetic moments cancel. The material has a macroscopic magnetic moment only when there is spin-polarization, i.e., a majority of the spins orient themselves in the same direction. If all of the spins point in the same direction, the material is called a ferromagnet. This kind of macroscopic orientation is possible if the spins interact in a way which makes them face the same direction. Even in this case, raising the temperature will introduce randomness in the orientation of the spins and at some specific point, the Curie temperature (T_C), the macroscopic order is lost and the ferromagnetic properties disappear.

After the discovery of ferromagnetic (In,Mn)As [21], other DMS materials based on III-V semiconductors were soon realized and DMS research focused on this group of materials. However, despite the vast theoretical effort to understand these materials, open questions still remain. The types of magnetic interactions between the magnetic elements can be different for different materials and no universally accepted model of DMS magnetism exists [6, 8, 22–24]. The most severe obstacle preventing the use of DMS's in applications has been their generally low Curie temperatures. Due to this, much of the research has been devoted to finding a diluted magnetic semiconductor where ferromagnetism remains at room temperature.

(Ga,Mn)As has been one of the most extensively studied DMS's [25–27] due to its relatively high Curie temperature, and it is often regarded as the prototype DMS material where the magnetic interactions are mediated by delocalized holes [28]. Typically the Curie temperatures of the epitaxially grown (Ga,Mn)As samples are about 110 K [29, 30] and a brief annealing can increase T_C to as high as 170 K due to outflow of Mn interstitials [31, 32]. However, long-time annealing reduces the Curie temperature once again [33, 34]. This phenomenon is explained as a Mn cluster formation process in Publication **IV**.

(Ga,Mn)N has also received much attention [6, 35–38] after it was theoretically predicted to have a Curie temperature above 300 K [8]. However, the growth of this material is not as well controlled as that of (Ga,Mn)As. The experimental T_C values range from zero to hundreds of Kelvins [39–41] and the variations have been speculated to be due to formation of second phases or Mn clusters [42–51]. Due to these difficulties, the mechanisms of magnetic interactions and the microscopic structure of the material have been poorly understood. These issues are addressed in Publications **I–III** where the influence of Mn cluster formation on the Curie temperature is investigated.

2.2 Anisotropic wet chemical etching of silicon

Anisotropic wet chemical etching of Si is a fabrication method where a sample of crystalline Si is exposed to an etchant solution (usually an alkali) that chemically removes (etches) the material. As the etch rate depends on the direction (anisotropy), the process can sculpt complex structures. Currently, the most commonly used anisotropic etchants are KOH and TMAH [tetramethylammonium-hydroxide, $(CH_3)_4NOH$]. On the microscopic level, etching is a process where the Si atoms on the H-terminated [52–54] Si surface are removed due to being attacked by the molecules in the etchant. According to the generally accepted model of wet chemical etching, the removal process of a Si atom is divided to oxidation and etching steps [55, 56]. In the chemical oxidation step, a hydrogen atom terminating a dangling bond on the Si surface is replaced by a hydroxide

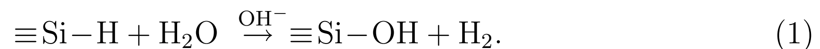

$$\equiv \mathrm{Si}-\mathrm{H} + \mathrm{H_2O} \overset{\mathrm{OH^-}}{\rightarrow} \equiv \mathrm{Si}-\mathrm{OH} + \mathrm{H_2}. \quad (1)$$

Here $\equiv$Si denotes a surface Si sharing three bonds with bulk Si atoms. This weakens the silicon back bonds and allows additional water molecules to remove the Si atom in the etching step

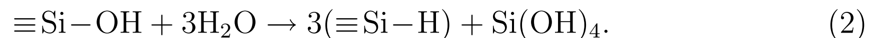

$$\equiv \mathrm{Si}-\mathrm{OH} + 3\mathrm{H_2O} \rightarrow 3(\equiv \mathrm{Si}-\mathrm{H}) + \mathrm{Si(OH)_4}. \quad (2)$$

(Similar reaction equations hold for the cases where some of the surface silicons only bond with one or two other Si atoms.) Since the rate of oxidation depends strongly on the local bond structure of the Si atom, the process is highly anisotropic. Atomistically, this means that Si atoms at kink sites are removed more rapidly than those on steps, which are likewise more reactive than the atoms forming terraces. On the macroscopic level this results in some crystallographic orientations etching rapidly while others, such as (111), are fairly inert [57].

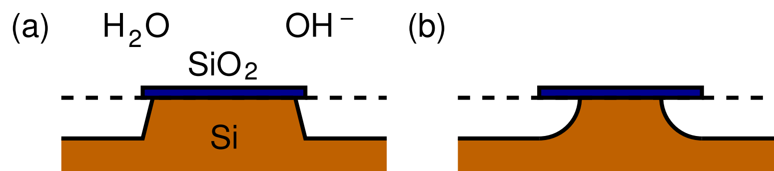

Figure 2.2: In (a) anisotropic etching, nearly perfect geometrical shapes are obtained while (b) isotropic etching results in round shapes.

During anisotropic etching, the rapidly etched surface orientations are quickly consumed by the etchant and the resulting structures are in general bound by the stable, slowly etching surfaces. In a device manufacturing process, specific parts of the surface are protected from the etchant by oxide or nitride masks. This way the anisotropy can be used as an advantage to create nearly ideal three-dimensional geometric shapes, as shown in Figure 2.2. Also, any protrusions extending from smooth surfaces usually contain active kink and step sites and are also removed in the etching process. So ideally, anisotropic etching should produce surfaces that are smooth even on the atomic level, making it a powerful tool in micromachining [54]. However, non-idealisms like etchant inhomogeneities [2,58], hydrogen bubbles [3, 59–61] and impurities [61–63] can locally disturb the etching process and lead to rough features such as pits [63], zig-zags (long straight ridges separated by V-shaped valleys) [2, 64, 65], step bunches (surface steps of more than one atomic layer) [2, 66] or hillocks [67–69].

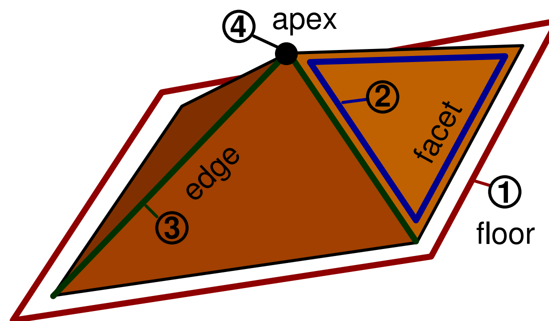

Figure 2.3: Etch hillocks have the shape of a square or a trapezoidal pyramid. The hillock structure can form if the floor (1) is etched rapidly while the hillock itself is stable at the facets (2), the facet edges (3) and the apex (4). [**VI**]

Hillock formation on the Si(110) surface is one of the most complex of the roughness inducing processes during etching and its theoretical understanding has been incomplete. It is understood that in general, etch hillocks can form if the surface itself is etched rapidly while the apex, facets and facet edges of the hillock are stable (see Figure 2.3) [18, 68]. On the other hand, it is also experimentally known that the presence of Cu impurities in the etchant, even in parts per billion (ppb) concentrations, can lead to the appearance of these hillocks [62]. (In industrial etching, such contamination can be present in the etchants used or get deposited on the Si wafers during surface cleaning.) This suggests that the Cu atoms stabilize the otherwise unstable hillock apices, and this is most likely due

to pinning, or micromasking, by impurities adsorbed on the Si surface. However, the exact structure of the hillocks, the relative stability of their various parts and the role of Cu or other impurities in their stabilization have not been previously addressed via direct simulations. In addition to the effect of Cu, experiments have also demonstrated that the presence of Pb lowers the etch rate without changing the morphology, while other metal impurities have no effect on the etching process [62]. The mechanisms causing the various impurities to act differently are also unknown.

In order to explain the formation of the hillocks and the role of Cu impurities in this process, the adsorption energetics of Cu on the H-terminated Si surface are studied in Publication **V** and the hillock formation process under the influence of impurities is analyzed in Publication **VI**. A more complete picture of the role of metal impurities is presented in Publication **VII**, where Pb, Mg and Ag impurities are studied in addition to Cu.

3 Calculations at the atomic scale

Physical properties of materials and molecules are due to the atomic nuclei and electrons they consist of, and the goal in first principles calculations is to deduce these properties by solving the fundamental quantum mechanical equations governing the behavior of these particles. Unfortunately, quantum mechanical problems are computationally very demanding. There are many approximate schemes for calculating the energy and electronic structure of systems at the atomic scale and the method must be chosen according to the required accuracy and available computational resources. Some of the most commonly used first principles computation techniques are based on the density-functional theory (DFT), as the theory leads to a formulation which is reasonably accurate in practical calculations while being efficient enough to be able to handle systems of some hundreds or even thousands of atoms [70, 71]. In this thesis, DFT was used for calculating magnetic interactions of Mn impurities as well as the energies and structures of Mn clusters in the DMS material (Ga,Mn)N. It was also applied to the calculation of adsorption energies of Cu, Pb, Ag and Mg as well as the cluster formation energies of Cu and Pb on H-terminated Si surfaces.

3.1 Density-functional theory

The energy eigenstates of a system of electrons[1] are given by the Schrödinger equation

$$\hat{H}\Psi(\mathbf{r}_1,\sigma_1;\ldots;\mathbf{r}_N,\sigma_N) = E\Psi(\mathbf{r}_1,\sigma_1;\ldots;\mathbf{r}_N,\sigma_N), \tag{3}$$

where Ψ is an N-body wave function and σ_i are the electron spin z-components ($\pm\hbar/2$, or $\uparrow$, $\downarrow$) and $\mathbf{r}_i$ are the positions of the electrons. $\hat{H}$ is the Hamiltonian operator which can be written (in Hartree atomic units) as

$$\begin{aligned}\hat{H} &= \hat{T} + \hat{V}_{\text{ext}} + \hat{V}_{\text{ee}} \\ &= -\frac{1}{2}\sum_i^N \nabla_i^2 + \sum_i^N V_{\text{ext}}(\mathbf{r}_i) + \frac{1}{2}\sum_{i\neq j}\frac{1}{|\mathbf{r}_i - \mathbf{r}_j|},\end{aligned} \tag{4}$$

where $\hat{T}$, $\hat{V}_{\text{ext}}$ and $\hat{V}_{\text{ee}}$ are the kinetic energy, external potential energy and electron-electron interaction operators, respectively.

[1]Since the atomic nuclei are massive when compared to electrons, they are often treated as fixed particles that create an external potential. This is the Born-Oppenheimer approximation.

The central premise of DFT is to ignore the full wave function Ψ and work on the three dimensional spin densities

$$n_\sigma(\mathbf{r}) = N \sum_{\sigma_2,\ldots,\sigma_N} \int \mathrm{d}^3 r_2 \ \ldots \mathrm{d}^3 r_N \ |\Psi(\mathbf{r},\sigma;\mathbf{r}_2,\sigma_2;\ldots;\mathbf{r}_N,\sigma_N)|^2 \tag{5}$$

instead. This is justified for calculation of ground state (gs) properties by the Hohenberg-Kohn theorems [72] which state that the variational principle holds for the density $\mathbf{n} = [n_\uparrow, n_\downarrow]$ — i.e. there exists an energy functional $E[\mathbf{n}]$ which gives the correct ground state energy for $\mathbf{n}_{\mathrm{gs}}$ and a higher energy for other densities — and that the ground state wave function is a functional of the ground state density, $\Psi_{\mathrm{gs}} = \Psi[\mathbf{n}_{\mathrm{gs}}]$.

In practice, the spin densities are calculated using the Kohn-Sham scheme [73,74]. The idea is to map the many-electron problem to a group of non-interacting one electron equations in an effective external potential V^σ_{KS}:

$$\left[-\frac{1}{2}\nabla^2 + V^\sigma_{\mathrm{KS}}[\mathbf{n}](\mathbf{r})\right] \psi^\sigma_i(\mathbf{r}) = \varepsilon^\sigma_i \psi^\sigma_i(\mathbf{r}) \tag{6}$$

$$n_\sigma(\mathbf{r}) = \sum_i |\psi^\sigma_i(\mathbf{r})|^2. \tag{7}$$

Here $\psi^\sigma_i = \psi^\sigma_i[\mathbf{n}](\mathbf{r})$ are effective Kohn-Sham orbitals used for determining the spin densities, not real wave functions. On the one hand, we know that the ground state density minimizes the total energy with the constraint of fixed number of electrons with up and down spins. Using Lagrange multipliers this can be written in the variational form $\delta\big[E[\mathbf{n}] - \sum_\sigma \mu_\sigma \int \mathrm{d}^3 r \ n_\sigma(\mathbf{r})\big] = 0$ and it leads to the Euler equations $\delta E/\delta n_\sigma = \mu_\sigma$. On the other hand, if we consider the system of non-interacting electrons, the energy is simply given by the non-interacting kinetic energy

$$T_0 = \sum_{i,\sigma} \int \mathrm{d}^3 r \ \psi^{\sigma *}_i(\mathbf{r}) \left(-\frac{1}{2}\nabla^2\right) \psi^\sigma_i(\mathbf{r}) \tag{8}$$

and the effective potential, leading to Euler equations $\delta T_0/\delta n_\sigma + V^\sigma_{\mathrm{KS}} = \mu_\sigma$. If we define the exchange-correlation energy via

$$E[\mathbf{n}] = T_0[\mathbf{n}] + \int \mathrm{d}^3 r \ n(\mathbf{r}) V_{\mathrm{ext}}(\mathbf{r}) + \frac{1}{2}\int \mathrm{d}^3 r \, \mathrm{d}^3 r' \ \frac{n(\mathbf{r})n(\mathbf{r}')}{|\mathbf{r}-\mathbf{r}'|} + E_{\mathrm{xc}}[\mathbf{n}], \tag{9}$$

where $n(\mathbf{r}) = n_\uparrow(\mathbf{r}) + n_\downarrow(\mathbf{r})$, comparing the Euler equations and (9) fixes the

effective Kohn-Sham potential as

$$V_{\mathrm{KS}}^{\sigma}[\mathbf{n}](\mathbf{r}) = V_{\mathrm{ext}}(\mathbf{r}) + \int \mathrm{d}^3r' \, \frac{n(\mathbf{r}')}{|\mathbf{r}-\mathbf{r}'|} + \frac{\delta E_{\mathrm{xc}}}{\delta n_{\sigma}}, \tag{10}$$

where $\delta E_{\mathrm{xc}}/\delta n_{\sigma} = V_{\mathrm{xc}}^{\sigma}[\mathbf{n}](\mathbf{r})$ is the exchange-correlation potential.

The formulation of DFT is in principle exact and all the difficulties of many-body interactions have been hidden in the exchange-correlation potential. However, sophisticated approximations for the exchange-correlation are computationally heavy and one must find a balance between the necessary accuracy and affordable computation time when choosing the proper treatment.

3.2 Implementations of the theory

In addition to the exchange-correlation functional, one must also choose how to describe the Kohn-Sham orbitals and decide on how to handle the electron–nucleus interactions when doing numerical calculations. Since DFT is a widely used technique, several different implementations exist. In this thesis, the VASP (Vienna Ab-initio Simulation Package) [75] and SIESTA (Spanish Initiative for Electronic Simulations with Thousands of Atoms) [76, 77] codes have been used for the study of DMS materials and Si surfaces, respectively. Of these two codes, VASP is considered to be more accurate while SIESTA is more efficient especially for large systems.

Exchange-correlation functionals

In the original formulation of the Kohn-Sham theory, the exchange-correlation was handled using the local density approximation (LDA)

$$E_{\mathrm{xc}}^{\mathrm{LDA}}[\mathbf{n}] = \int \mathrm{d}^3r \; n(\mathbf{r}) e_{\mathrm{xc}}(\mathbf{n}(\mathbf{r})), \tag{11}$$

where e_{xc} is the exchange-correlation energy density of the uniform electron gas. The approximation is valid for systems where the electron density is slowly changing, but in practice it gives reasonable results even for single atoms where the density is not homogeneous.

The so-called generalized gradient approximation (GGA) is the most common class of improved exchange-correlation functionals. In GGA, also the density gradients

are used for calculating the exchange-correlation energy

$$E_{\mathrm{xc}}^{\mathrm{GGA}}[\mathbf{n}] = \int \mathrm{d}^3 r \; f^{\mathrm{GGA}}(\mathbf{n}, \nabla \mathbf{n}) \tag{12}$$

and several different parametrizations f^{GGA} exist, such as PW91 [78], PBE [79] and BLYP [80, 81]. Although LDA and GGA are usually adequate, they have shortcomings. For instance, semiconductor band gaps calculated using these functionals tend to be too narrow [70]. More advanced functionals have been designed to further correct LDA and GGA, such as meta-GGA [82], on-site Coulomb corrected LDA + U [83, 84] and self-interaction corrected SIC [85]. Also so-called hybrid functionals have become increasingly popular. These functionals work by combining parts of various exchange-correlation functionals and the Hartree-Fock (exact) exchange in order to balance the shortcomings of any single functional [86, 87]. In this work, the functionals PW91, LDA + U [**I**–**III**] and PBE [**V**–**VII**] have been used.

Basis functions and k-points

The VASP code uses a plane wave basis where the Kohn-Sham orbitals are expressed using an expansion

$$\psi^{\sigma}(\mathbf{r}) = e^{i\mathbf{k}\cdot\mathbf{r}} \sum_{\mathbf{G}} c^{\sigma}_{\mathbf{k},\mathbf{G}} e^{i\mathbf{G}\cdot\mathbf{r}}, \tag{13}$$

where $\mathbf{k}$ is a wave vector from the first Brillouin zone and $\mathbf{G}$ are reciprocal lattice vectors. The sum is truncated for some $|\mathbf{G} + \mathbf{k}| > G_{\mathrm{cut}}$ and adjusting this cut-off allows one to easily control the accuracy of the expansion.

A linear combination of atomic orbitals (LCAO) approach is adopted in SIESTA. This means that the orbitals are expanded in a spherical harmonic type basis connected to each atom. These basis functions are also strictly cut at some specified distance. This increases the locality, which enables the calculation of individual molecules, wires or slabs without unwanted interactions with periodic images. Calculating large systems also becomes faster when basis functions corresponding to atoms far from each other do not overlap. However, controlling convergence in LCAO is not as simple as tuning the energy cut-off in a plane wave basis and several parameters must usually be fine-tuned to ensure accuracy. In addition, removing or adding atoms changes the basis and this may lead to basis set superposition errors (BSSE) requiring additional corrections [88].

Regardless of the used basis, evaluation of physical quantities in crystals and other periodic systems often requires calculation of integrals over the Brillouin zone. This is done by numerical integration using sets of **k**-points in the reciprocal space, chosen according to the Monkhorst-Pack scheme [89].

Nuclear potentials

The Coulomb potential between a nucleus and an electron is of the form $1/r$ and it diverges when the separation r gets short. This results in rapidly oscillating electronic wave functions near the nuclei which are difficult to describe using truncated basis set expansions. In order to circumvent this problem, SIESTA uses pseudopotentials [90] while VASP allows the use of the projector augmented wave (PAW) method [91–93].

Pseudopotentials equal the real potentials when viewed far away from the nuclei, but at short distances the diverging potential is replaced by a smooth function. This also smooths out the wave function oscillations near the nuclei making these pseudo wave functions numerically easier to handle. Usually the electrons of an atom are divided into core and valence electrons. The core electrons are thought to be inert and so they are ignored in the Kohn-Sham scheme while their screening effect is incorporated into the pseudopotentials. The valence electrons are treated fully in the calculations. Since the chemical properties of atoms depend on the behavior of the electronic wave functions in the interstitial region, the pseudopotential approach is justified e.g. in bond calculations. In the SIESTA calculations presented in this work, the norm-conserving Troullier-Martins parametrization of pseudopotentials was used [94].

PAW shares the core and valence region philosophy of pseudopotentials but implements it in a more sophisticated manner. The idea is to construct a linear transformation $\hat{T}$ between smooth auxiliary functions $|\tilde{\psi}\rangle$, for which a plane wave expansion converges rapidly also near the nuclei, and real physical states $|\psi\rangle = \hat{T}|\tilde{\psi}\rangle$. Physical operators can also be transformed accordingly, $\langle\psi_i|\hat{Q}|\psi_j\rangle = \langle\tilde{\psi}_i|\hat{T}^\dagger\hat{Q}\hat{T}|\tilde{\psi}_j\rangle = \langle\tilde{\psi}_i|\tilde{Q}|\tilde{\psi}_j\rangle$, allowing the calculation of matrix elements using the easy-to-handle auxiliary functions, leading to modified Kohn-Sham equations. In essence, PAW provides a direct correspondence between the auxiliary functions and the exact Kohn-Sham equations — something that does not exist for the pseudo wave functions of the pseudopotential method.

The PAW transformation is constructed as follows. Near the nuclei positioned at $\mathbf{R}$, in areas denoted by $\Omega_{\mathbf{R}}$, the wave functions are expanded in atomic partial waves (spherical harmonics) $|\phi_{\alpha,\mathbf{R}}\rangle$. Since the wave functions need to be smoothed only near the nuclei, the transformation is of the type

$$\hat{T} = \hat{I} + \sum_{\mathbf{R}} \hat{T}_{\mathbf{R}}, \tag{14}$$

where $\hat{T}_{\mathbf{R}}$ have an effect only inside $\Omega_{\mathbf{R}}$. Now, smooth auxiliary partial waves $|\tilde{\phi}_{\alpha,\mathbf{R}}\rangle$ are chosen so that

$$\hat{T}_{\mathbf{R}}|\tilde{\phi}_{\alpha,\mathbf{R}}\rangle = |\phi_{\alpha,\mathbf{R}}\rangle - |\tilde{\phi}_{\alpha,\mathbf{R}}\rangle \tag{15}$$

$$\phi_{\alpha,\mathbf{R}}(\mathbf{r}) = \tilde{\phi}_{\alpha,\mathbf{R}}(\mathbf{r}), \quad \mathbf{r} \notin \Omega_{\mathbf{R}} \tag{16}$$

and projectors $\langle\tilde{p}_{\alpha,\mathbf{R}}|$ are defined allowing the expansion of auxiliary wave functions using the auxiliary basis

$$|\tilde{\psi}\rangle = \sum_{\alpha} \langle\tilde{p}_{\alpha,\mathbf{R}}|\tilde{\psi}\rangle|\tilde{\phi}_{\alpha,\mathbf{R}}\rangle. \tag{17}$$

Combining (14), (15) and (17) yields the transformation

$$\hat{T} = \hat{I} + \sum_{\alpha,\mathbf{R}} \Big(|\phi_{\alpha,\mathbf{R}}\rangle - |\tilde{\phi}_{\alpha,\mathbf{R}}\rangle\Big) \langle\tilde{p}_{\alpha,\mathbf{R}}|. \tag{18}$$

Once the auxiliary expansion and the projectors have been defined, applying the transformation operator is straightforward.

Self-consistency iteration

Calculating the effective potential from (10) requires knowledge of the density $\mathbf{n}$. However, in order to solve the spin densities from (6) and (7) one needs the effective potential. In practice, this problem is overcome using a self-consistency iteration. Some initial guess is made for the density, the effective potential is determined based on it, and a new density is solved from the potential. This is repeated with the new density — or some mixture of the new and old densities — until the change in the total energy between iteration steps becomes small enough, indicating that all of the equations (6), (7) and (10) are satisfied simultaneously.

Setup of the calculated systems

Both the DMS and Si systems studied in this work were calculated in periodic supercells. The (Ga,Mn)N material was treated as bulk wurtzite [**I**–**III**]. The data used for modeling (Ga,Mn)As [**IV**] came from similar calculations in the bulk zinc-blende structure [1, 95, 96]. The Mn atoms were always placed on Ga interstitial sites and remained relatively immobile in geometric optimization. The H-terminated Si surfaces were modeled as (111), (112) and (221) oriented slabs of three to four Si layers, with periodicity in only two dimensions [**V**–**VII**]. The metal impurities in these calculations were placed on various surface sites from where they were allowed to find local energy minima.

4 Simulating macroscopic phenomena

At the macroscopic scale, the behavior of physical systems is normally governed by classical mechanics[2] and statistical physics. The so-called Monte Carlo (MC) methods, which rely on the use of random numbers, are naturally suitable for statistical analysis [97]. However, Monte Carlo techniques may in some cases also be used for simulating the kinetics of non-equilibrium processes. In this thesis, the equilibrium MC technique was used for calculating the Curie temperatures of the diluted magnetic semiconductor materials, and also to estimate the Mn cluster size distributions in (Ga,Mn)N. Kinetic MC (KMC) was mostly used for etching simulations. Lattice KMC results of Mn diffusion in (Ga,Mn)As [98] were also used as a starting point for T_{C} calculations in Publication **IV**. This Section introduces the used MC methods and presents the physical models to which these simulation schemes are applied.

4.1 Equilibrium Monte Carlo

Phase space sampling

The macroscopic properties of a system in equilibrium can be described using statistical physics and ensemble theory. Let us denote the phase space of possible system states by Ω and the normalized probability of the system to be in state $\mathbf{x} \in \Omega$ by $\rho(\mathbf{x})$. For a system described by the Hamiltonian H, the canonical probability density is then given by the Boltzmann distribution

$$\rho(\mathbf{x}) = \frac{1}{Z} e^{-H(\mathbf{x})/k_{\mathrm{B}}T}, \tag{19}$$

with $Z = \mathrm{Tr}\, e^{-H/k_{\mathrm{B}}T}$ being the canonical partition function. Now in principle, the macroscopic averages for such a system are obtained by integrating over the phase space

$$\langle A \rangle = \mathrm{Tr}\, \rho A = \frac{1}{Z} \mathrm{Tr}\, A e^{-H/k_{\mathrm{B}}T}. \tag{20}$$

However, such integrals can be incredibly complex and straightforward numerical integration methods are unable to handle them. The integration can be carried

[2]Classical theory is valid when the relevant length scales are longer than the de Broglie wavelength, which is microscopic.

out by using Monte Carlo methods to sample points in the phase space, $\{\mathbf{x}_i\} \subset \Omega$, according to the distribution $\rho(\mathbf{x})$. By doing so, the ensemble average is simply approximated by an arithmetic average [97]

$$\frac{1}{Z}\mathrm{Tr}\, Ae^{-H/k_\mathrm{B}T} \approx \frac{\sum_i^N e^{-H(\mathbf{x}_i)/k_\mathrm{B}T} A(\mathbf{x}_i)/\rho(\mathbf{x}_i)}{\sum_i^N e^{-H(\mathbf{x}_i)/k_\mathrm{B}T}/\rho(\mathbf{x}_i)} \tag{21}$$

$$= \frac{1}{N}\sum_i^N A(\mathbf{x}_i). \tag{22}$$

This procedure is called importance sampling since it emphasizes the statistically important regions of Ω. The $A(\mathbf{x}_i)$ values typically fluctuate only moderately making the average (22) converge rapidly as N increases.

Markov chains

In order to formulate algorithms that realize the importance sampling of points in the phase space, we introduce stochastic processes known as Markov chains [97]. A Markov chain is a collection of random variables $\{\mathbf{x}_i\}$ so that the probability distribution of a variable $\mathbf{x}_{i+1}$ depends on the value of the previous one, $\mathbf{x}_i$. For simplicity, let us consider the case where variables can obtain values only from a finite set of states $\{\mathbf{y}^j\}$. For such finite Markov chains we can define probability vectors π_i so that the element $(\pi_i)^j$ holds the probability that the variable $\mathbf{x}_i$ is in the state $\mathbf{y}^j$. Since the probabilities for π_{i+1} only depend on their previous values, π_i, a transition matrix P links the vectors together

$$\pi_{i+1} = P\pi_i. \tag{23}$$

If the process is aperiodic and if starting from one state it can reach any other (i.e. it is ergodic), a unique limiting distribution exists

$$\Pi = \lim_{i\to\infty} \pi_i = \lim_{n\to\infty} P^n \pi_0 \tag{24}$$

for any initial distribution π_0.

The transition matrix elements P_{kj} can also be interpreted as transition rates from state $\mathbf{y}^j$ to $\mathbf{y}^k$, $R(j \to k)$, when jumping from one random variable to the next. Since the limiting distribution is static, the in- and outflow of probabilities must

balance out

$$\Delta\Pi^j = \sum_k \left[R(k \to j)\Pi^k - R(j \to k)\Pi^j\right] = 0. \tag{25}$$

This is certainly satisfied if

$$\frac{R(j \to k)}{R(k \to j)} = \frac{\Pi^k}{\Pi^j} \tag{26}$$

for all j and k. Equation (26) is called the detailed balance condition and it provides a connection between the transition probabilities and the limiting distribution. More precisely, we only need to adjust the ratios of transition probabilities between all pairs of states in order to fix the limiting distribution. Therefore, to sample the Boltzmann distribution (19), we only need to generate a chain of states $\{\mathbf{x}_i\}$ so that the transition probabilities when jumping from $\mathbf{x}_i$ to $\mathbf{x}_{i+1}$ obey

$$\frac{R(j \to k)}{R(k \to j)} = \frac{e^{-H(\mathbf{y}^k)/k_{\mathrm{B}}T}}{e^{-H(\mathbf{y}^j)/k_{\mathrm{B}}T}} = e^{-\Delta E_{j\to k}/k_{\mathrm{B}}T}. \tag{27}$$

Monte Carlo algorithms

Knowing the condition (27) that our Monte Carlo method should satisfy, we can finally formulate actual algorithms for generating the chain of states $\{\mathbf{x}_i\}$ in (22). One of the simplest Monte Carlo algorithms is the Metropolis scheme [99], which in essence works as follows. Being in the state $\mathbf{x}_i = \mathbf{y}^j$, one picks a test state $\mathbf{y}^k$ and calculates the energy difference $\Delta E = E^k - E^j$. The test state is then accepted, $\mathbf{x}_{i+1} = \mathbf{y}^k$, with the probability $P = \min(1, e^{-\Delta E/k_{\mathrm{B}}T})$ and rejected otherwise, $\mathbf{x}_{i+1} = \mathbf{y}^j$. This procedure is then repeated.

The Metropolis algorithm has been widely used since it can be applied to a variety of systems. For instance, in the case of spins, the test state is usually obtained by randomly rotating one spin. However, the algorithm is not very efficient. If the probabilities P are in general low, most of the time the algorithm does nothing. Additionally, near a second order phase transition, like the Curie point, the correlation length ξ, measuring the length scale of ordered structures, diverges. This leads to so-called critical slowdown in the Metropolis scheme, since more and more MC iterations are needed to produce uncorrelated states.

The Wolff method [100], an extension of the Swendsen-Wang technique [101], is designed to overcome the critical slowdown in spin systems. As such, it is quite efficient near the Curie point but it does not share the generality of the Metropolis

scheme. The algorithm begins by randomly choosing a spin as a seed for a cluster. It then proceeds by finding the spins that interact with the seed and joining them to the cluster with specific probabilities. When a new spin joins, the process is repeated so that all spins interacting with the cluster are given a chance to join. Once all interacting spins have been tested, all the spins in the cluster are reflected with respect to some randomly chosen plane, generating a new state.

Simulation of magnetic impurities

The model for magnetic impurities developed and implemented for this thesis is based on the classical Heisenberg Hamiltonian [102], where the spins of the impurities are approximated as classical unit vectors with pairwise exchange couplings. Since the impurities do not sit in an ordered lattice, but form a more or less random distribution of clusters, it is meaningful to separate the interactions of impurities in the same and different clusters. Denoting the kth spin in the ith cluster by $\mathbf{s}_i^k$ we may write

$$\begin{aligned} H &= -\sum_{(i,k;j,k')} J_{ij}^{kk'} \mathbf{s}_i^k \cdot \mathbf{s}_j^{k'} && (28) \\ &= -\sum_{(i;j)} \sum_{k,k'} J_{ij}^{kk'} \mathbf{s}_i^k \cdot \mathbf{s}_j^{k'} - \sum_i \sum_{(k;k')} J_{ii}^{kk'} \mathbf{s}_i^k \cdot \mathbf{s}_i^{k'}, && (29) \end{aligned}$$

where $(\cdot\,;\cdot)$ denotes a sum over pairs. The normalized spin of the ith cluster is given by the sum

$$\mathbf{S}_i = \frac{1}{n_i} \sum_k^{n_i} \mathbf{s}_i^k \tag{30}$$

with n_i being the number of impurities in the cluster. Approximating the intercluster coupling coefficients by

$$J_{ij}^{kk'} = J_{ij} = J(\mathbf{r}_{ij}) n_i^{-1} n_j^{-1}, \quad i \neq j, \tag{31}$$

where $\mathbf{r}_{ij}$ is the vector between cluster centers i and j, (29) can be rewritten for the cluster spins as

$$H = -\sum_{(i;j)} J(\mathbf{r}_{ij}) \mathbf{S}_i \cdot \mathbf{S}_j - \sum_i E_i, \tag{32}$$

where the internal energy of the ith cluster is denoted E_i. This separation of inter- and intracluster interactions is schematically demonstrated in Figure 4.1.

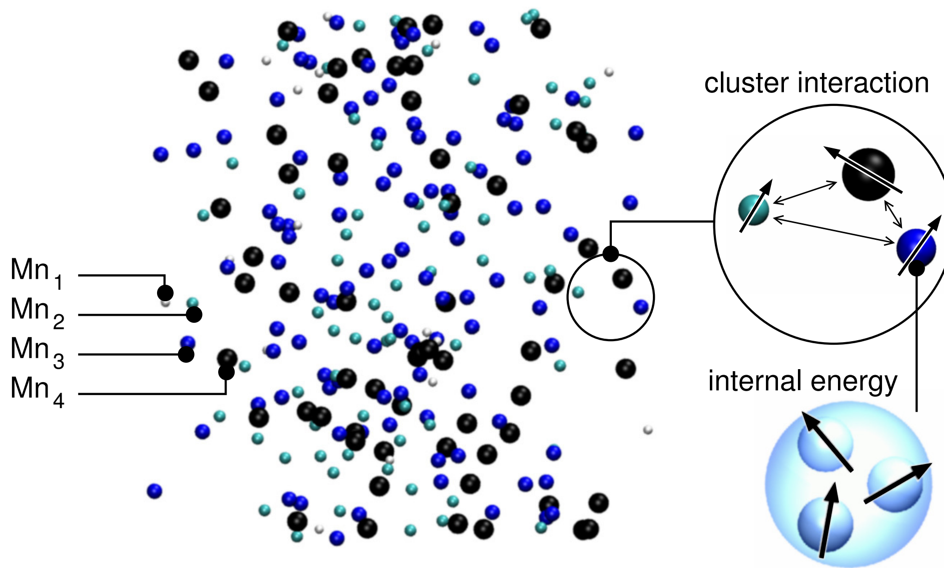

Figure 4.1: Classical spin model used for simulating diluted magnetic semiconductors (the host semiconductor is not shown). The spins of magnetic impurities are grouped in clusters (sizes shown with varying colors) and the inter- and intracluster interactions are treated separately. [**III**]

The above derivation is merely a regrouping of the classical Heisenberg Hamiltonian. However, it turns out that pairwise interactions do not properly describe the magnetic coupling of Mn atoms in the same cluster [103, **II**, **III**] and therefore it is appropriate to treat E_i as a general function. For simplicity, this function is assumed to only depend on the size of the cluster and the length of the classical cluster spin, $E_i = E_{n_i}(S_i)$.

The derived spin Hamiltonian is connected to atomistic calculations by a parametrization of the exchange coupling functions J_{ij} and the internal energy functions E_i according to first principles spin-flip energies (see Section 5.1 and Publication **III**). The Monte Carlo calculations for the model are carried out using an alternating Wolff–Metropolis hybrid algorithm. The Wolff method is used for sampling the cluster spins $\mathbf{S}_i$ efficiently, keeping the internal degrees of freedom of the clusters frozen. In order to avoid ignoring the internal structure of the clusters, the individual impurity spins $\mathbf{s}_i^k$ within the clusters are rotated using the Metropolis scheme. The applied hybrid method constantly switches between these two modes. The validity and efficiency of the implementation was tested by analyzing well-known classical Ising and Heisenberg models [104].

Phase transitions

The Curie temperature is a point of a second degree phase transition, where the spontaneous magnetization M of a ferromagnet disappears as the temperature T is increased. However, since simulations are necessarily done in finite systems, the magnetization of a simulated system does not disappear in one well defined point but instead it approaches the zero level smoothly. A rough estimate for T_C can be found by interpolating the magnetization vs. temperature curve. An accurate determination of T_C and distinction between a first and a second phase transition requires the use of finite size scaling methods, though. One such technique is the cumulant crossing scheme [105], where the fourth order cumulant $U_L(T) = 1 - \langle M^4 \rangle / 3 \langle M^2 \rangle^2$ is measured for different simulated system sizes L. As L increases, the value of U_L approaches two different constants, U_- and U_+, for $T < T_C$ and $T > T_C$, respectively. At $T = T_C$, the cumulant obtains an intermediate value regardless of L. Thus, the Curie point can be found with good accuracy at the intersection point of U_L with different L [97].

4.2 Kinetic Monte Carlo

In the importance sampling of phase space done in equilibrium Monte Carlo, it does not matter how the states are picked as long as the probabilities obey the detailed balance condition (26). In kinetic Monte Carlo (KMC), however, time is associated with the chain of generated states and each jump from a state, $\mathbf{x}_i$, to the next, $\mathbf{x}_{i+1}$, should describe a meaningful physical process. Similarly, a transition rate $R(j \to k)$ corresponds to the physical occurrence rate of the process leading from the configuration of state $\mathbf{y}^j$ to that of state $\mathbf{y}^k$. In short, KMC works by stochastically advancing the development of the system according to predetermined occurrence rates of processes. [106]

Stochastic dynamics

Consider some arbitrary state $\mathbf{y}^j$. In principle, we should be able to reach any other state $\mathbf{y}^k$ from this configuration, but in a complicated system almost all of these transition processes are highly complex and can be physically divided into simpler subtransitions occurring one after another: $\mathbf{y}^j \to \mathbf{y}^k$ becomes $\mathbf{y}^j \to \mathbf{y}^l \to \mathbf{y}^k$

etc. Continuing this line of thought, we are finally left with a group of indivisible transitions so that all other transitions can only occur as a sequence of these simple ones. Now, assume that the simple processes are uncorrelated and of the Poisson type with transition rates $R_k = R(j \to k)$. In that case, the waiting time for a particular process is exponentially distributed $\tau_k \sim \exp(R_k)$ and the probability that the process does not occur in time t is given by $P_k(t) = \exp(-R_k t)$. Then the probability that no processes occur in time t is $P_\sigma(t) = \prod_k P_k(t) = \exp(-\sum_k R_k t) = \exp(-R_\sigma t)$, where $R_\sigma = \sum_k R_k$ is the total rate of all simple processes. That is, the waiting time for anything to happen is also exponentially distributed, $\tau_\sigma \sim \exp(R_\sigma)$ with an average of $1/R_\sigma$. Although KMC simulations can be done with e.g. the Metropolis method, where one tries to advance the system with constant time steps, this result allows a backwards approach: It can be stochastically decided how long it takes for anything to happen, and the particular process that occurs after this period of time can be chosen separately [107]. This way each KMC step results in the realization of exactly one process and no computational time is wasted in rejections.

The time advancement between processes is given by the waiting time for any process τ_σ. Using uniform random numbers $\zeta \in (0, 1]$, this is realized by

$$\Delta t = \tau_\sigma = -\frac{\ln \zeta}{R_\sigma}. \tag{33}$$

Choosing the processes and updating the system are more complicated tasks. Yet, they need to be fast since most of the computational time will be spent in these activities. The KMC simulations in this thesis use optimized tree search algorithms [108] for finding the processes. Basically, a random number $\zeta \in (0, 1]$ is chosen and the process $\mathbf{y}^j \to \mathbf{y}^k$ for which $\sum_i^{k-1} R_i < \zeta R_\sigma \leq \sum_i^k R_i$ is picked. In order to find the right index k quickly, a tree structure of partial sums is kept in memory at all times. Having found the correct process, the system is advanced accordingly and the process rates are updated where necessary before the next process is chosen. The tree-search algorithms are very efficient KMC-search methods and they are especially useful when the set of values the process rates R_k can obtain is large [2].

Simulation of etching with impurity exposure

The etching simulator used in this this thesis is based on the Fortran 90 version of the TAPAS (Three-dimensional Anisotropic Processing at All Scales) KMC code

by M. A. Gosálvez [18, 109, 110], with considerable modifications and extensions implemented by the author, most notable additions being algorithms for simulating adsorption of metal impurities, a triangulation generator for the Si surface, and a four-index classification scheme for Si atoms [111], as described below. The validity of the implemented algorithms was tested by measuring impurity distributions on simple test surfaces and by comparing etching results between different versions of TAPAS. Since etching is a non-equilibrium process consisting of well-defined atomic events, kinetic Monte Carlo is well suited for describing it.

The simulated systems consist of an atomic Si lattice and impurities which may either be in the etchant (i.e. "free") or adsorbed on the Si surface. The simple KMC processes are chosen to be the removals of single Si atoms from the surface, and the adsorptions and desorptions of single impurity atoms. The Si atoms on the surface are classified according to their local neighborhoods by counting the numbers of first and second nearest neighbor Si atoms. These neighbors are in addition distinguished according to whether they are on the surface or in the bulk [111]. So, each Si atom is categorized by four indices describing the type of terrace, step or kink the atom is in [112] and the removal rates are decided accordingly. The etchant solution is not simulated as such, but the etching conditions are taken into account in the Si removal rates.

The etchant also acts as a limited reservoir of free impurities. That is, the impurities in the etchant do not have a real location and they can adsorb anywhere on the surface. The impurity-silicon interface is constructed as a triangulation of the H-terminated Si surface. The positions of the hydrogen atoms covering the surface are projected to a 2D point cloud from which a Delaunay triangulation is generated using the Bowyer-Watson method [113, 114]. In the simulations, each triangle is considered to be a potential adsorption site for the impurities. These sites are classified according to the shapes of the triangles and the impurity adsorption and desorption rates can be set site specifically. The construction is schematically presented in Figure 4.2.

The adsorbed impurities are treated as pinning agents which block the etching process at the nearby Si atoms. In the simulator, this is handled by decreasing the removal rates of the Si atoms connected to an impurity. Once an impurity has adsorbed, it may desorb either thermally or due to underetching, i.e., if a Si atom to which it is connected is removed. Finally, the impurities may form clusters on the surface. In the simulations this is realized by increasing the adsorption rates

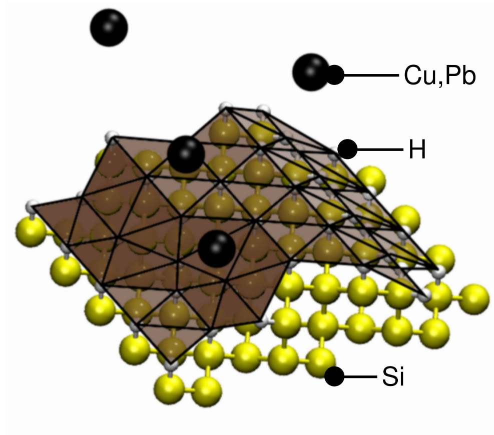

Figure 4.2: The etching model consists of an atomistic Si lattice as well as free and adsorbed impurity atoms. A triangulation of the Si surface acts as an interface between the silicon and impurity subsystems. [**VI**]

at the sites next to those already occupied by impurities.[3] Mechanisms such as surface diffusion which can contribute to cluster formation [115] are not explicitly included in the simulation model. However, the purpose of the applied method is to create semirealistic clusters in order to investigate the development of the Si surface in their presence, not to accurately simulate the behavior of the impurities. Therefore, these omissions are justified.

The KMC simulations of etching are connected to the atomistic adsorption simulations by estimating the site specific impurity adsorption and desorption rates from first principles activation energies, E, as $\nu \exp(-E/k_{\mathrm{B}}T)$ where ν is a parameter (see Section 5.2 and Publication **VI**). The method for simulating cluster formation is a simplified one, and so in Publication **VI** morphologies are studied as a function of a varying interaction strength. In Publication **VII**, the interaction is set to semiquantitatively mimic the behavior seen in the atomistic calculations. The Si removal rates have been adjusted according to experimental data [18, 57].

[3] This is called "interaction enhanced adsorption" in Publication **VI**, where other phenomenological schemes for simulating cluster formation are also tested.

5 Microscopic interactions and formation of clusters

5.1 Structure and magnetism of Mn clusters

Structure and formation of clusters in (Ga,Mn)N

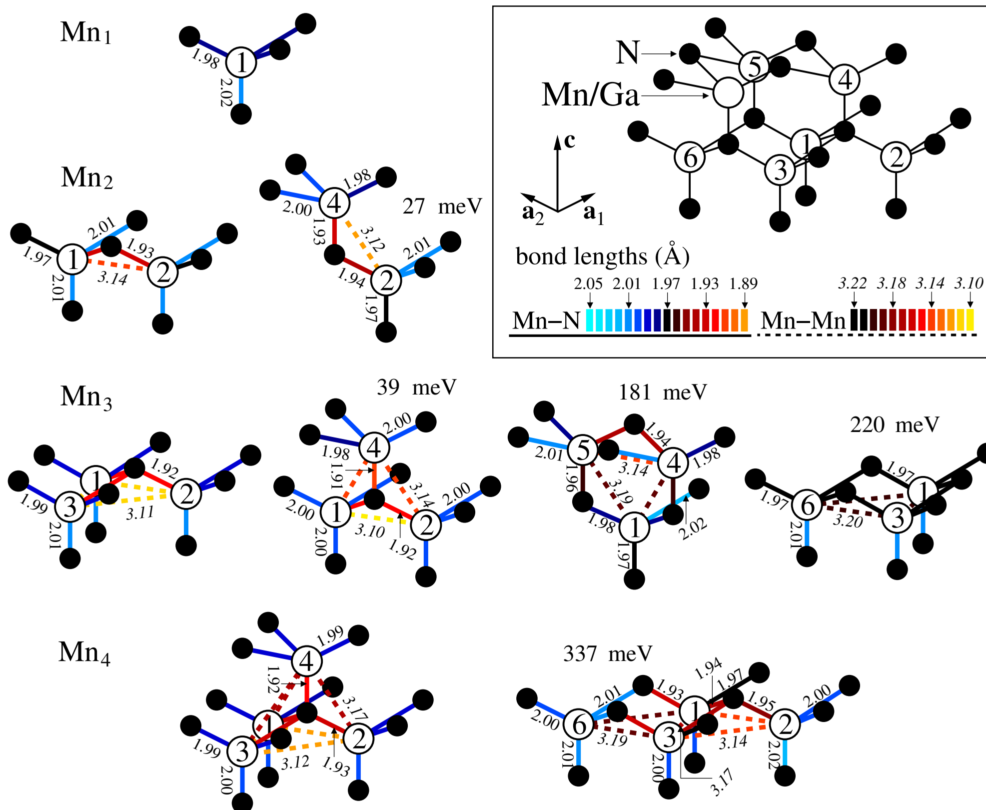

Figure 5.1: Calculated structures of Mn complexes in (Ga,Mn)N. The energies are given with respect to the most favored structure of equal size (the leftmost clusters). Bond lengths are shown with colors. Numbering of the atoms shows which Ga atoms in the structure shown in the inset are replaced by Mn. [**III**]

When only a few Mn atoms are considered, the energetically most favorable Mn cluster configurations in (Ga,Mn)N are the ones where the substitutional Mn atoms gather around a single N atom. Calculated cluster structures are shown in Figure 5.1 from monomers to tetramers. It is seen that once the Mn atoms share a neighboring N atom, the Mn–Mn separations shorten and small, compact clusters form. The relaxations in bond lengths are smaller in the cases where the Mn

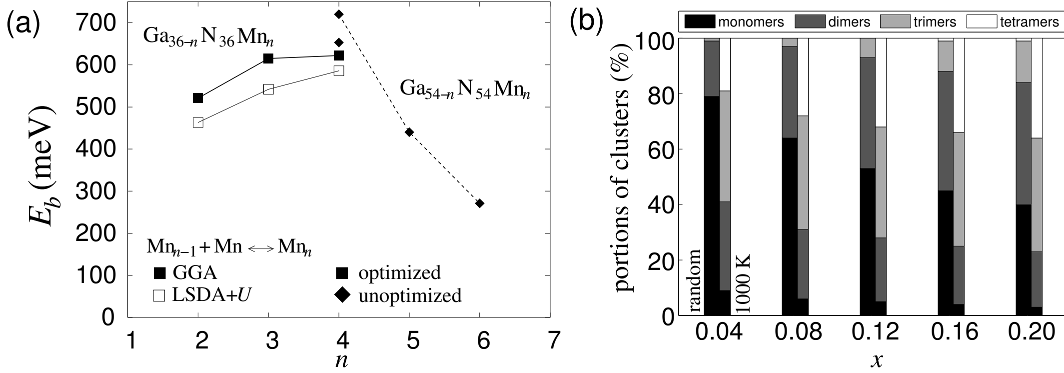

Figure 5.2: (a) The binding energies of Mn atoms in n-mers. [**III**] (b) Average portions of clusters in (Ga,Mn)N for random (left columns) and 1000 K equilibrium (right columns) Mn distributions. Here, clusters are defined as Mn atoms sharing the same neighboring N atom. [**II**]

atoms are not situated around one and the same nitrogen, and the energies of these structures are somewhat higher.

The tendency of the Mn atoms to form clusters is estimated in Figure 5.2 (a) by comparing the energy of a cluster of n Mn atoms to those of a cluster of $n-1$ atoms plus a monomer, $E_b = E(\text{Mn}_{n-1} + \text{Mn}) - E(\text{Mn}_n)$. These binding energies grow as a function of cluster size n up to tetramer formation, for which E_b is about 0.6 eV (depending on the calculation scheme) demonstrating an effective attraction between the Mn atoms. For clusters larger than tetramers, the binding energies decrease. This suggests that although joining individual Mn atoms in these larger clusters is still energetically favored, it is best for the Mn atoms to form small clusters. It is an indication that the cluster formation may be limited to the small complexes of only a few atoms, at least if the Mn concentration is low. Due to these considerations, we focus on clusters where the Mn atoms share a single central N atom, naturally limiting the maximum cluster size to tetramers.

The distribution of the Mn cluster sizes at different Mn concentrations x (as in $\text{Ga}_{1-x}\text{Mn}_x\text{N}$) is shown in Figure 5.2 (b) for (Ga,Mn)N lattices with either completely random Mn substitution or in equilibrium at 1000 K (obtained using a Metropolis MC calculation). Since even in the random distribution a considerable portion of the Mn clusters hold two or three atoms, it is evident that these small clusters are present (Ga,Mn)N. Furthermore, nearly all of the Mn atoms form clusters in equilibrium due to the energy gain in cluster formation. The cluster distribution in real (Ga,Mn)N is likely something between these extremes.

The structures of Mn clusters in (Ga,Mn)As have been calculated in [1, 95] using the same first principles code as used here, VASP, and the obtained binding energies behave qualitatively similarly to those in (Ga,Mn)N, showing a maximum for tetramer formation. Furthermore, in [98] the kinetics of substitutional Mn_{Ga} atoms and Mn vacancies have been investigated using the CASINO lattice KMC code [116] resulting in cluster distributions similar to those shown in Figure 5.2.

Magnetic coupling

We estimate the strength of magnetic coupling between individual or clustered Mn atoms by calculating the spin-flip energies ($\Delta E = E_{\uparrow\downarrow} - E_{\uparrow\uparrow}$) between spin configurations where one or more spins have been flipped (cf. [117]). The ground states of isolated Mn clusters in (Ga,Mn)N are always found to be ferromagnetic, the spins facing the same direction. The energy required for flipping the spin of one Mn atom in a cluster decreases from 300 meV in dimers to 120 meV in tetramers as the cluster size grows, but still, these are quite high energies indicating a relatively strong coupling between the Mn atoms. The coupling between clusters is estimated in a similar fashion, and like the Mn atoms, also all clusters show a ferromagnetic coupling regardless of the cluster sizes and intercluster distances [**I**, **II**, **III**]. However, the analysis of the intercluster coupling is complicated since the interactions are fairly long-ranged and periodic images are present in the calculations.

To get an estimate on the strength and spatial behavior of the cluster-cluster exchange coupling, we fit the Heisenberg Hamiltonian (29) to the calculated spin-flip energies (via simulated annealing optimization [118]) by introducing phenomenological coupling functions of the form

$$J(r) = \frac{A}{r^\alpha} + B(r - r_1)e^{-\beta(r-r_2)^2}, \tag{34}$$

where r is the distance between clusters.[4] The first term describes the decaying tail of the coupling while the latter oscillatory term accounts for the strong coupling at intermediate cluster separations (cf. [37, 38, 96, 119]). The function is cut at some distance r_{cut}, so that clusters whose separation exceeds this limit do not interact. Although the exchange coupling between Mn clusters is expected to be anisotropic, i.e., its strength depends not only on the length, but also on the

[4] Out of several functions tested, this form yielded the best fit while being relatively simple.

direction of the cluster separation vector **r** [120, 121], the fitting procedure turns out to be reasonably successful even when the anisotropy is ignored.

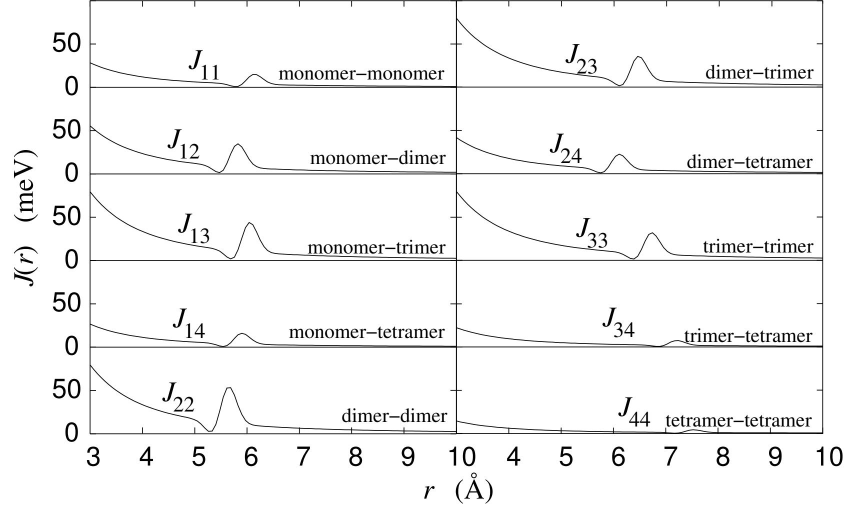

Figure 5.3: Exchange coupling $J_{n_i n_j}(r)$ between Mn clusters in (Ga,Mn)N. [**II**]

For (Ga,Mn)N, the intercluster exchange coupling depends explicitly on the sizes of clusters as shown by the fitted $J_{n_i n_j}(r)$ functions in Figure 5.3 ($r_{\text{cut}} = 13$ Å). Due to the size dependence, all the functions have been fitted separately. However, since carrying out extensive first principles calculations for each cluster pair at various separations is not feasible, the shape of the oscillatory part is assumed to be similar in all cases to reduce the number of free parameters in (34) [**II**, **III**]. The simplified fitting procedure results in coupling functions with relatively high uncertainties in their pointwise values. However, the important qualitative properties of the DFT spin-flip energies are preserved: The coupling is clearly strongest for dimers and

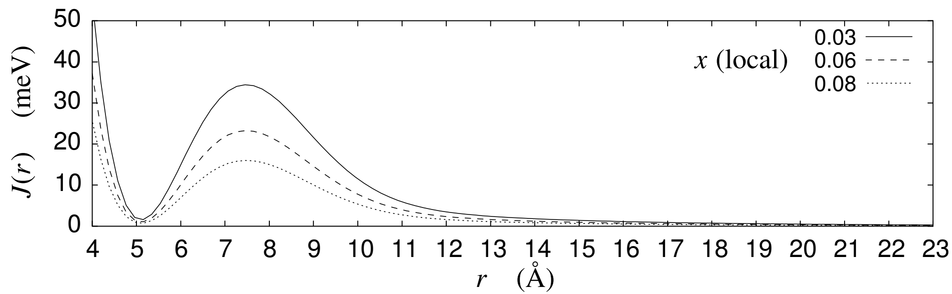

Figure 5.4: Exchange coupling $J_x(r)$ between Mn clusters in (Ga,Mn)As. [**IV**]

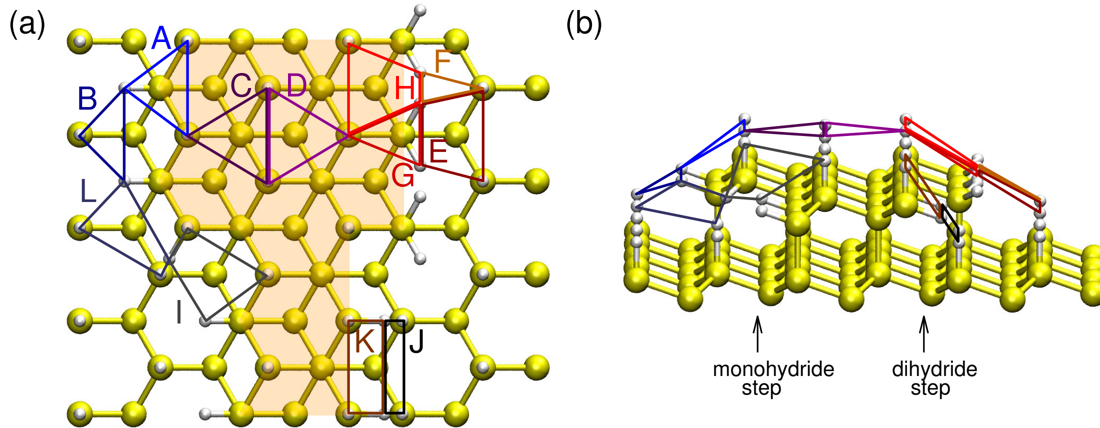

Figure 5.5: The most common types of possible adsorption sites on the H-terminated Si-surface viewed from (a) top-down and (b) side perspectives: monohydride steps (A, B), horizontal (E–H) and vertical (K, J) dihydride steps, (111) terraces (C, D) and kinks (I, L). [**VII**]

trimers and weak for tetramers, indicating that the clustering state of the Mn atoms directly affects the magnetism of the material.

A similar fit is done for (Ga,Mn)As based on the spin-flip calculations of [1, 95]. In this case, the coupling is expected to be independent of the size of the clusters [96], but it depends on the local Mn concentration [38, 120, 122, 123].[5] Therefore the (Ga,Mn)As exchange function is multiplied by a linear scaling function, $J_x(r) = f(x)J(r)$, to account for the concentration dependence. The fitted coupling function is plotted in Figure 5.4 ($r_{\text{cut}} = 23$ Å). The most important differences to (Ga,Mn)N, besides the lack of the cluster size dependence, are the longer range and lower maximum of the interaction.

5.2 Metal impurities on the H-terminated Si surface

Adsorption of impurities

While the Mn atoms in (Ga,Mn)N and (Ga,Mn)As are in the bulk, substituting Ga atoms, the metal impurities relevant for etching are on a Si surface. Furthermore, these impurities can adsorb and desorb. Therefore, one must examine the

[5] Also the coupling in (Ga,Mn)N may depend on the Mn concentration, but estimating the effect for all cluster pairs would require much more data from first principles calculations.

Table 5.1: Adsorption energies of metal impurities on various surface sites on the H-terminated Si surface (in eV). Two adsorption states are found for Pb: (A) denotes a weakly adsorbed state and (R) denotes a strongly bonded state where a Si−H + Pb → Si−Pb−H reaction has occurred. [**V**, **VII**]

site	Cu	Pb (A)	Pb (R)	Mg	Ag
A	−0.55	−0.49	−1.22	-	-
B	−0.89	−0.48	−1.22	-	-
C	−0.77	−0.50	−1.26	−0.04	−0.12
D	−1.17	−0.39	−1.26	-	-
E	−1.01	−0.49	−2.12	-	-
F	−1.43	-	−1.56	+0.42	−0.31
G	−0.63	−0.54	−1.64	-	-
H	−1.39	-	−2.12	-	-
I	−1.34	-	−1.43	-	-
J	−1.10	-	−1.46	-	-
K	−0.50	-	−1.46	-	-

adsorption of single impurities before cluster formation can be studied. Since the Si surface changes during etching, many different surface structures may appear. Furthermore, many types of surface sites, where impurities may possibly adsorb, exist on the various terraces, steps and kinks. The most common ones are shown and labeled with letters in Figure 5.5.

Table 5.1 lists calculated adsorption energies for Cu and Pb (the active metals according to experiments [62]) as well as Ag and Mg on the H-terminated Si surface. The electronic densities of the adsorbed atoms on the step site F are

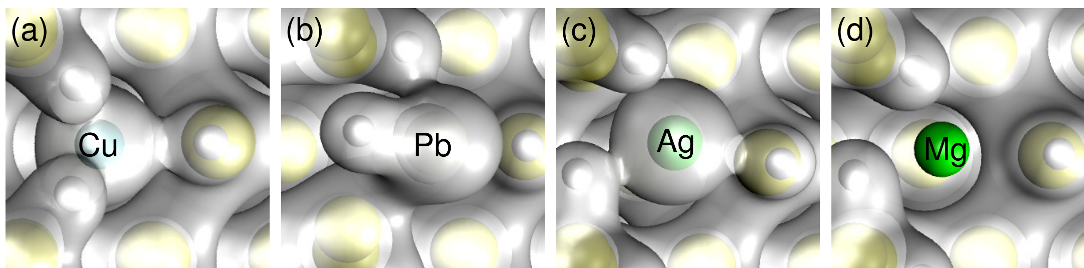

Figure 5.6: The valence electron densities of adsorbed (a) Cu, (b) Pb, (c) Ag and (d) Mg atoms on the F site. The densities are drawn at an isosurface of 0.014 e/Å^3 for Pb and 0.019 e/Å^3 for the other impurities. [**VII**]

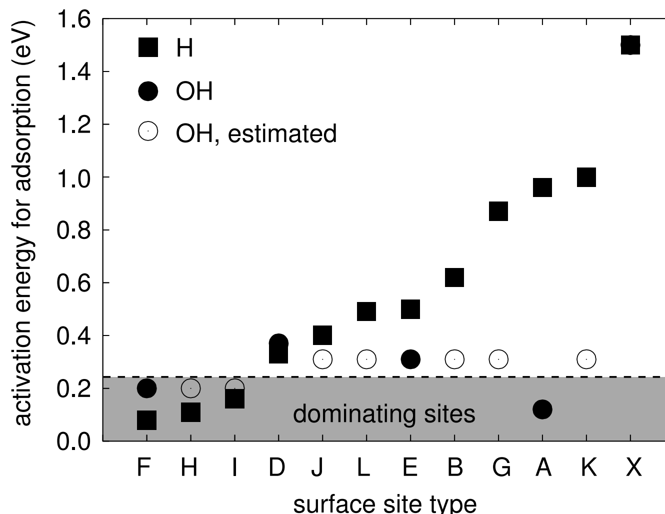

Figure 5.7: Adsorption activation energy hierarchy for Cu on various surface sites on H- and OH-terminated Si surfaces. Adsorption is most likely on the sites with a low activation energy. [**VI**]

shown in Figure 5.6. For Cu, the adsorption energies are highly site specific, and the energetically most favored adsorption sites for Cu are found on the dihydride steps and kinks.[6] The adsorption energy is roughly speaking proportional to the number of bonds the Cu can form with the surface, making the adsorption site shown in Figure 5.6 (a) especially favorable. Such strong site specificity is not seen with Pb. However, Pb can adsorb in two ways: by bonding with the H atoms on the surface or by replacing the H's in a Si−H + Pb → Si−Pb−H reaction, denoted by (A) and (R), respectively, in Table 5.1. Of these two, the (A) states have relatively low adsorption energies while the (R) states are always quite strongly bonded to the surface. Figure 5.6 (b) shows the (R) state. The other metals, Ag and Mg, adsorb only weakly in agreement with experiments according to which only Cu and Pb affect the etching process.

In order to estimate the kinetics of Cu and Pb adsorption, the activation energies for adsorption and desorption are calculated for a few test sites (D and F for Cu and D for Pb). For Cu, the peaks of the desorption barriers are about 1.5 eV above the energy of the adsorption state. Assuming this for other sites as well leads to the adsorption barrier hierarchy in Figure 5.7. In the case of Pb, no energy barrier is found between the free atom state and the weakly adsorbed state. Also

[6]If OH-groups are present, Cu can bond with the oxygen and adsorb anywhere [**V**].

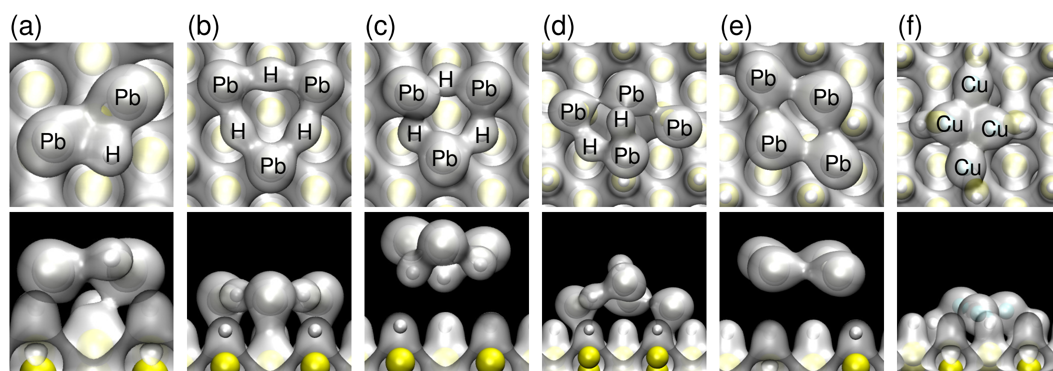

Figure 5.8: Structures and electron densities of (a) a Pb_2H dimer, (b) a Pb_3H_3 trimer, (c) a Pb_3H_3 trimer on a H-terminated surface, (d) a Pb_4H_2 tetramer, (e) a Pb_4 tetramer, and (f) a Cu_4 tetramer. The densities are drawn at an isosurface of 0.014 e/$Å^3$ for Pb and 0.019 e/$Å^3$ for Cu. [**VII**]

the activation energy of the H replacing reaction for a weakly adsorbed Pb is only 0.3 eV. Thus, it is very easy for the Pb atoms to adsorb and react, and the uniform adsorption energies suggest that they can do this anywhere on the surface.

Structure and formation of Cu and Pb clusters

Since Pb can adsorb in two different ways, the number of structures that can form increases rapidly as the number of available Pb atoms increases. Figures 5.8 (a)–(e) show some of the energetically favored ones on a (111) terrace up to the size of four Pb atoms. Since the adsorption energies of clusters on a fully H-terminated surface are very low, about -0.1 eV [Figs. 5.8 (c) and (e)], in order to be strongly attached to the surface, the Pb atoms in the cluster must bond directly with the Si atoms on the surface [Figs. 5.8 (a), (b) and (d)]. The H atoms removed from the surface become a part of the Pb clusters. However, as the cluster size grows to four Pb atoms, the strongly bonded state [Fig. 5.8 (d)] cannot find a symmetric ground state like trimers and dimers can [Figs. 5.8 (a) and (b)], and the weakly adsorbed purely metallic cluster [Fig. 5.8 (e)] becomes energetically as favorable as the strongly adsorbed state. For the smaller clusters, the energy of the metallic state is much higher than that of the strongly bonded configurations. This suggests that if the size of the Pb complex grows, ultimately the metallic cluster becomes the favored state. For Cu, such behavior is not seen, since Cu bonds strongly with the surface without disturbing the H atoms [Fig. 5.8 (f)].

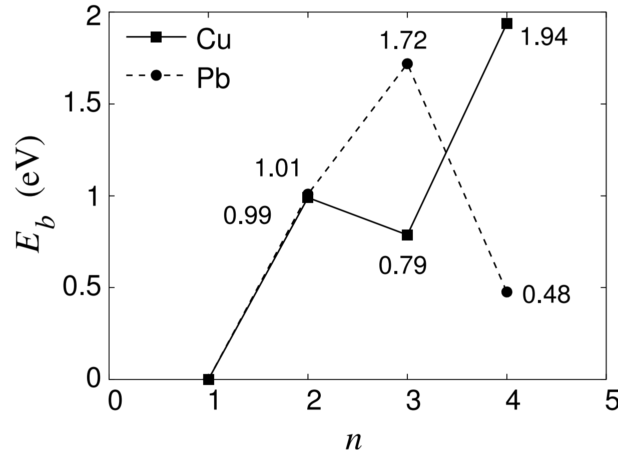

Figure 5.9: Binding energies of Cu and Pb atoms in n-mers. [**VII**]

The binding energies of Cu and Pb atoms in clusters of n atoms are shown in Figure 5.9, calculated by comparing the energies of systems with a Si slab and a cluster of n, $n-1$, 1 or no impurity atoms, $E_b = [E(\mathrm{X}_{n-1})+E(\mathrm{X})]-[E(\mathrm{X}_n)+E(\emptyset)]$ (X = Cu or Pb). The graph is analogous to Figure 5.2 (a). For Pb, the symmetric trimer [Fig. 5.8 (b)] is an especially favored structure with a high binding energy, but in tetramers the binding is much weaker. As was argued in the case of the Mn atoms in (Ga,Mn)N, this suggests that Pb should favor the formation of small clusters more than that of large aggregates. (Or, as discussed above, the larger Pb clusters adopt a metallic state which adsorbs only weakly and thus can mask the Si surface only very briefly.) The binding energies of Cu, on the other hand, increase greatly for n values 2 and 4 (compared to $n-1$) and decrease only slightly for $n = 3$, indicating that Cu should be eager to form clusters. This is a clear qualitative difference in the behavior of Cu and Pb and an indication why these metals affect the etching process differently.

6 Macroscale effects of impurities and clusters

6.1 Effect of Mn microstructure on Curie temperature

Using the cluster spin model (29) with the phenomenological exchange parameters (34), determining the Curie temperature by MC calculations is straightforward. The resulting T_C's are plotted in Figure 6.1 as a function of Mn concentration for random and 1000 K equilibrium cluster distributions, as in Figure 5.2 (b). Also T_C values estimated by mean-field approximations (MFA's) are shown for various lattices.

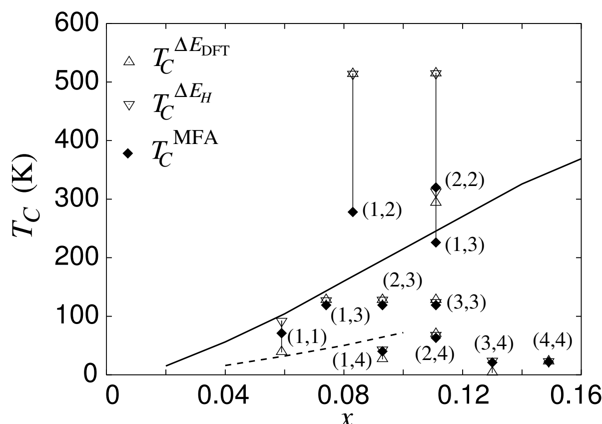

Figure 6.1: Calculated Curie temperatures of (Ga,Mn)N as a function of Mn concentration. Values obtained from both MFA (points) and MC calculations (lines) are shown. The numbers in parenthesis show the sizes of clusters in the lattices (MFA). The solid and dashed lines correspond to random and 1000 K equilibrium distributions (MC). [**III**]

The Curie temperatures of a random distribution are seen to increase nearly linearly and reach room temperature at around $x = 0.14$ — a high, but not a totally unfeasible level. In the equilibrium configuration, though, T_C is much lower, less than 100 K for $x = 0.10$. As the only difference between these systems is the stage of cluster formation, it is evident that the Mn microstructure plays a crucial role in determining the magnetic properties of the material. Furthermore, since growing (Ga,Mn)N and controlling the microscopic structure is difficult, the lowering of T_C caused by clustering may be a source of the wildly varying experimentally measured T_C values. The MFA values [**I**, **III**] calculated either from a

sum of the fitted intercluster exchange parameters ($T_C^{MFA} = \sum_j J_{0j}/3k_B$) or from comparing the energies of ferromagnetic and antiferromagnetic spin configurations ($T_C^{\Delta E} = 2\Delta E/3k_B N$, N being the number of magnetic centers) agree relatively well with the more sophisticated MC calculations. In general, the MFA values are too high because local magnetic fluctuations and the internal structure of the magnetic clusters are neglected, but nonetheless they capture the T_C decreasing effect of cluster formation. Some of the $T_C^{\Delta E}$ values grossly overestimate the Curie temperature compared to the T_C^{MFA} or MC results, though, due to overemphasis of the strong short-ranged interactions (most notable for the monomer-dimer and dimer-dimer systems). Still, the fact that the $T_C^{\Delta E_{DFT}}$ values, calculated using the actual first principles spin-flip energies, are so close to the $T_C^{\Delta E_H}$ results, obtained by first estimating the spin-flip energies using the model Hamiltonian (29), demonstrates that the used model agrees with the first principles results quite well.

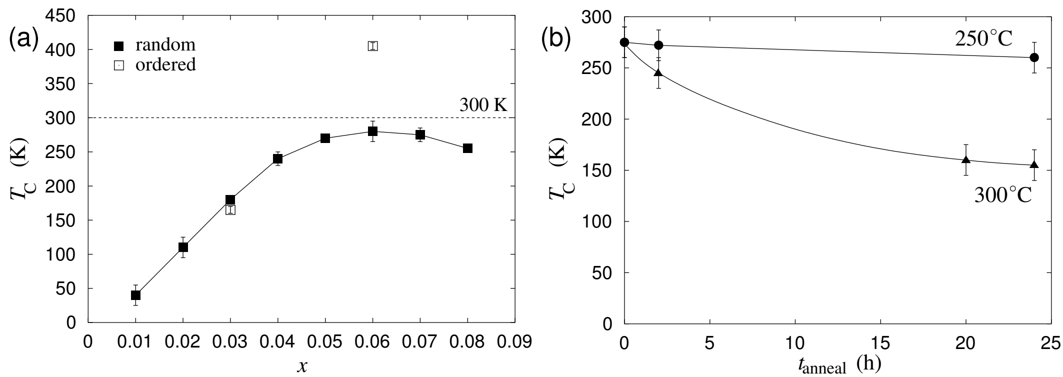

Figure 6.2: Calculated Curie temperatures of (Ga,Mn)As as a function of (a) Mn concentration and (b) anneal time. [**IV**]

Similarly, the Curie temperatures of (Ga,Mn)As with a random Mn distribution are plotted as a function Mn concentration in Figure 6.2 (a). Such a random distribution can be thought to mimic an as-grown sample after the outflow of Mn interstitials in short annealing. In this case, a maximum is reached in the Curie temperature at $x = 0.06$, somewhat below room temperature. The decrease in T_C beyond this point is due to both cluster formation and the decreasing exchange functions $J_x(r)$. The absolute value of the calculated maximum T_C is too high compared to experiments, since factors such as substitutional As_{Ga} and possibly remaining Mn interstitials are not considered here. However, the position of the calculated maximum agrees quite well with experiments [29, 30, 32]. Disorder is

seen to decrease the Curie point, since a high T_C of over 400 K is obtained for an ordered lattice on Mn monomers at this concentration.

To study the decrease in experimental Curie temperatures of (Ga,Mn)As during prolonged annealing, we also calculate the Curie temperatures of realistic Mn distributions, at $x = 0.06$, obtained by simulating the microstructure development using lattice KMC simulations [98]. The T_C's calculated for these structures as a function of annealing time are shown in Figure 6.2 (b). At 250 °C, the formation of Mn clusters is slow and so the Curie point drops by only a few Kelvins during 24 h of annealing. At a somewhat higher annealing temperature, 300 °C, cluster formation is rapid and T_C decreases tens of Kelvins in just two hours. After 24 h, the Curie temperature has decreased by almost one half. At this point the rate of decrease is slower than initially, since the microstructure does not evolve as dramatically anymore. Again, the calculated T_C values are much higher than the experimental ones, but otherwise the relative changes agree with those observed in experiments [33, 34]. Thus, the decreasing (Ga,Mn)As Curie temperature during long-time annealing can be attributed to the formation of small Mn clusters.

Cluster formation affects the Curie temperatures by three mechanisms. Firstly, the number of magnetic centers (i.e., clusters or single atoms) decreases as several magnetic elements are joined to form a single cluster, and the average distance between two magnetic centers increases when the density of these centers is reduced. Secondly, the magnetic clusters have internal degrees of freedom which individual magnetic elements lack. Thirdly, the interactions between the magnetic centers may be different for clusters of different sizes. If the ferromagnetic coupling decays as a function of separation, the first mechanism reduces T_C as clusters form. The second mechanism always decreases T_C, since it allows the total magnetic moments of the clusters to decrease due to fluctuations in their internal magnetic ordering. The third mechanism may either increase or decrease T_C. In (Ga,Mn)As, all clusters interact with the same strength and thus the third mechanism is in fact completely missing. In (Ga,Mn)N, the formation of dimers increases the interaction strength and the formation of tetramers kills it nearly entirely. Combining these effects, we see that cluster formation always decreases T_C in (Ga,Mn)As. In (Ga,Mn)N, the effects more or less cancel out in dimer formation, but the appearance of larger clusters, especially tetramers, is detrimental to the ferromagnetism of the material.

6.2 Influence of impurities on surface morphology

Etching simulations where no impurities are present do not lead to the appearance of trapezoidal hillocks on Si(110) surfaces. This is because even if a small hillock would appear due to a random fluctuation, its apex would be very reactive and the etchant would consume the structure from above. No hillocks develop even if non-interacting, adsorbing impurities are included in the simulation as pinning agents. An impurity atom adsorbed on the surface can prevent the removal of the Si atoms beneath it and so a hillock could in principle start growing, the stabilized Si atoms serving as the apex. However, the facets of the trapezoidal hillocks are approximately {311} oriented, as shown in the experimental and theoretical images of Figures 6.3 (a) and (b), and they have a low, yet noticeable etch rate compared to the (110) floor. Therefore, any single impurity on the apex of such a hillock will be removed due to underetching after a short while. At this point the stability of the apex is lost and the hillock is quickly destroyed.

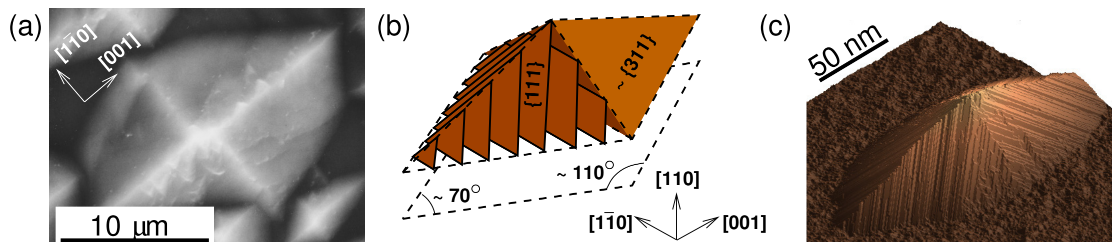

Figure 6.3: Trapezoidal hillocks seen on (110) surfaces: (a) an experimental SEM image [62], (b) the theoretical structure [18], and (c) the simulated structure. [**VI**]

If the impurities formed a cluster on the hillock apex, the removal of individual pinning agents would not lead to the immediate collapse of the hillock since a part of the cluster would remain as a micromask. Such behavior is actually expected for Cu, since we know from first principles calculations that the formation of Cu clusters on the H-terminated Si surface is energetically favorable. Indeed, when the formation of clusters is included in the simulation, the hillocks appear. The structure of the simulated hillocks, shown in Figure 6.3 (c), agrees with the experimental and theoretically expected ones, although, the size of the simulated hillock is much smaller than those seen in experiments. In Publication **VI**, different phenomenological models for driving Cu clustering have been tested. Though the

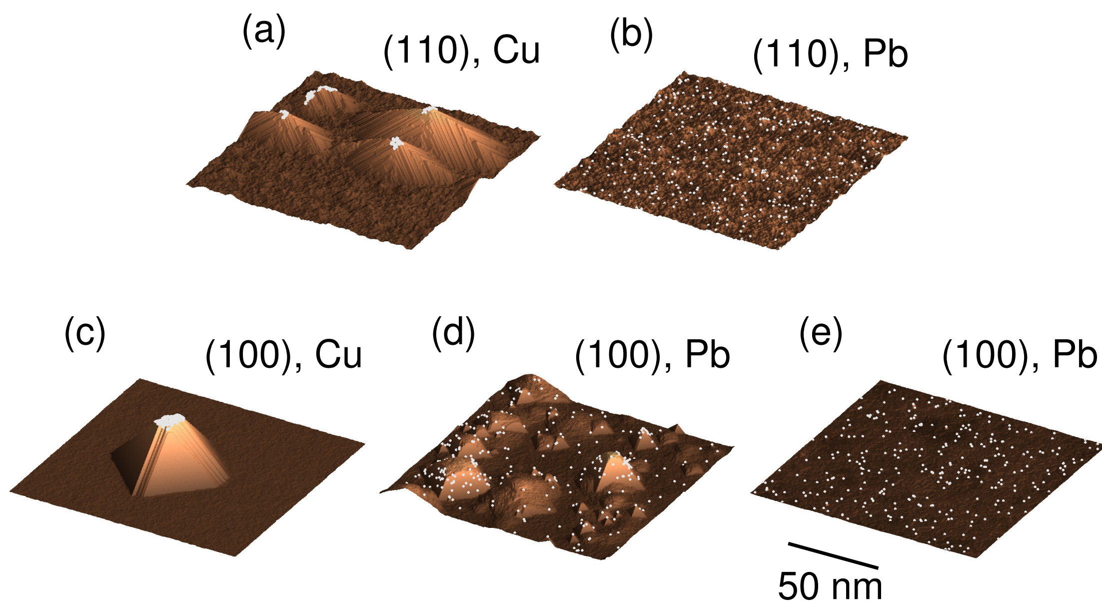

Figure 6.4: Morphologies of Si surfaces etched exposed to metal impurities: (110) at high [KOH] with (a) Cu and (b) Pb, and (100) at low [KOH] with (c) Cu and (d,e) Pb. In (d), the hillock edges are more stable than in (e). [**VII**]

applied methods result in quite different distributions of Cu atoms on the surface, the hillocks grown underneath Cu clusters had a very similar structure in all cases.

Since trapezoidal hillocks appear to be stabilized by impurity clusters, rather than individual impurities, the different cluster formation tendencies of Cu and Pb should be a major factor behind the different effects these impurities have on the etching process. This hypothesis is verified by KMC simulations of Cu and Pb. The resulting morphologies are shown in Figure 6.4 and the measured surface roughnesses and etch rates are plotted in Figure 6.5. Here, Cu is realized as an impurity experiencing site specific adsorption and an attractive impurity–impurity interaction, while Pb is treated as an impurity with uniform adsorption and no attraction. The Cu adsorption rates obey the hierarchy estimated form DFT results (Figure 5.7). However, the simulated morphologies are quite insensitive with respect to small changes in the adsorption rates, and once the impurities have a tendency to form clusters, it is sufficient that the few key sites Cu prefers on the surface are open for adsorption [**VI**].

As mentioned previously, Cu clusters act as micromasks on the apices of the trapezoidal hillocks on (110) [Fig. 6.4 (a)], but the individual Pb impurities cannot

stabilize the hillock structures [Fig. 6.4 (b)]. The formation of hillocks naturally increases the surface roughness considerably, but it also decreases the etch rate since the developing {311} facets etch slower than the (110) floor. Since Pb impurities do not induce hillock growth, their presence does not affect the surface roughness either. They do decrease the etch rate though, since every adsorbed Pb pins their neighboring Cu atoms. As the Pb atoms are constantly adsorbing and desorbing, their local pinning effect leads to an overall decrease in the average etch rate of the entire surface. All of these factors agree with the experimental observations [62].

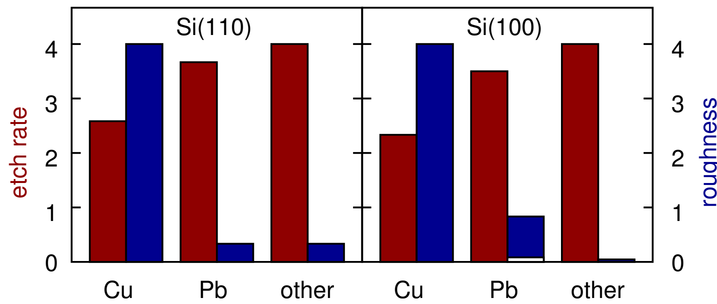

Figure 6.5: The simulated etch rate (left bars) and roughness (right bars) of (110) at high [KOH] and (100) at low [KOH] when exposed to different impurities, in arbitrary units. For Pb on (100), the white and blue bars correspond to the morphologies of Figs. 6.4 (e) and (d), respectively. [**VII**]

In addition to the trapezoidal hillocks seen on (110) at high etchant concentration, pyramidal hillocks appear on the (100) surface at low concentration [18].[7] Simulations of the (100) surface show that, like the trapezoidal ones, also the pyramidal hillocks can be stabilized by Cu clusters [Fig. 6.4 (c)]. Again, this leads to an increased surface roughness and decreased etch rate. The effect of Pb depends delicately on the etching conditions. The (111) facets of the pyramids are so stable that underetching is slow enough to allow individual impurities to stabilize the hillock apices for a short time [Fig. 6.4 (d)]. However, if the facet edges are made even slightly less stable, no hillocks are seen [Fig. 6.4 (e)]. In both cases the etch rate is lower than when no adsorbing impurities are present. The surface roughness is of course higher in the case where hillocks develop compared to when they do not (white bar in Fig. 6.5).

[7] At high concentration, the (110) floor etches rapidly as does the (100) floor at low concentration. Therefore, the hillocks appear on these surfaces in different etching conditions.

7 Conclusions

The first principles calculations of (Ga,Mn)N in Publication **I** demonstrated how the magnetic coupling between Mn clusters depends explicitly on the sizes of the clusters. Simple mean-field estimates even predicted that the formation of dimers could lead to Curie temperatures above room temperature. In Publication **II**, the distributions of cluster sizes in random and equilibrium configurations were calculated, showing that the formation of clusters is unavoidable and must therefore be taken into account when analyzing the material. More sophisticated estimates of the Curie temperature were calculated using Monte Carlo analysis of a cluster spin Hamiltonian. However, the very high T_C values obtained using the mean-field approach were not reached. In Publication **III**, the structure of Mn clusters was analyzed in more detail and the discrepancy between MFA and MC methods was explained to be mostly due to an overemphasis of the strong short range interactions in MFA. The cluster spin approach was also applied to (Ga,Mn)As in Publication **IV** in order to study the development of the Curie temperature during annealing.

In both (Ga,Mn)N and (Ga,Mn)As, the formation of Mn clusters is seen to considerably decrease the Curie temperatures. In the case of (Ga,Mn)N, in which controlling the microstructure is difficult, this may explain the wild variations in the experimentally observed magnetic properties. In (Ga,Mn)As, on the other hand, the observed decrease in Curie temperature during annealing can be directly attributed to the growth of Mn clusters. The calculated Curie temperatures of (Ga,Mn)As remain below room temperature for disordered systems, but the values for (Ga,Mn)N reach 300 K at a high Mn concentration. The semiquantitative agreement between the calculated and experimental T_C values of (Ga,Mn)As suggests that the applied cluster model succeeds in capturing the main factors affecting the Curie temperatures. Yet, as the predicted Curie points are still too high, the role of, for instance, structural defects needs to be taken into account in calculations, in addition to cluster formation [124–126]. Since e.g. vacancies are expected to reduce the Curie temperature, obtaining such high T_C's in real materials is difficult and better control over the microstructure of the materials is needed. Of course, it is also possible that other DMS materials may turn out to be better suited for applications than those examined in this thesis. In fact, new DMS materials with different dopants, such as Cr [127, 128], and other host semiconductors, for instance ZnO [129, 130], are being constantly studied.

The adsorption of Cu on the H- and OH-terminated Si surfaces was studied in Publication **V**, and the Cu atoms were seen to prefer adsorption on specific surface sites mostly found on dihydride steps and kinks, or near OH groups. Using the obtained Cu adsorption energy hierarchy and additional activation energy calculations, the adsorption kinetics of Cu were estimated and used in a KMC simulation of impurity contaminated Si etching in Publication **VI**. These simulations showed that etch hillocks appear on the (110) surface if there are stable pinning agents blocking the etching locally and protecting the hillock apices. In the case of Cu, the formation of clusters was seen to lead to such stable structures. A more complete picture of the influence of metal impurities was built in Publication **VII**, where also Pb, Ag and Mg were studied on a H-terminated surface. It was verified by first principles calculations that metals other than Cu and Pb do not adsorb on the surface, in agreement with the experimental observation that only Cu and Pb impurities affect the etching process. Furthermore, the results suggested that only small Pb clusters can adsorb on the surface while Cu can form large particles. Simulated etching based on this picture demonstrated that this difference in behavior between the two metals results in completely different macroscale development. Namely, the Cu clusters with long lifetimes can lead to the appearance of hillocks and slowly etching surfaces. The Pb impurities also lower the etch rate, but they do not stay on the surface long enough to stabilize large hillocks.

Understanding the origin of the rough surfaces developed during etching allows one to confront the problem and design better processes. In the cases where roughness is due to impurities, better control of impurity contamination could solve the problem. Other methods can also be found to prevent the adsorption of impurities — for instance, the roughening effect from having Cu in the etchant can be neutralized by a high concentration of Mg impurities [131]. As another example, stirring or adding surfactants in the etchant can improve surface quality [3, 61, 132, 133], especially by aiding the release of hydrogen bubbles from the surface.

The methods applied in this thesis contain several levels of approximations. First of all, unavoidable numerical inaccuracies result from the use of DFT and gradient corrected exchange-correction functionals. To handle these uncertainties, the DFT methods used in this work have been validated by testing various calculation schemes and functionals and by comparing with experiments [134, 135, **I**, **III**, **V**]. Secondly, the parametrization of the Monte Carlo methods using the limited first-principles data has required substantial approximations. However, the severity of

the induced errors depends on the sensitivity of the MC simulations. In DMS's, the calculated Curie temperatures are proportional to the exchange parameters J which in turn are proportional to the calculated spin-flip energies. So, even if the absolute values of the parameters are inaccurate, the relative T_C's of different configurations can be compared to study the effects of cluster formation as long as the relative values of the various J's can be trusted. In etching, the KMC results have been shown to be relatively stable against variations in the adsorption rates of impurities demonstrating that moderate numerical uncertainties should not affect the final conclusions [**VI**]. On the other hand, when the results are sensitive with respect to the parameters — as in (100) etching with Pb impurities — no certain conclusions can be made [**VII**].

Finally, there are simplifications in the Monte Carlo simulation models themselves. The KMC etching model is limited by the set of permitted processes, and it can be improved by including more details. Studying the processes themselves would require molecular dynamics simulations, though. The most notable simplification in the DMS simulations, is the use of the classical Heisenberg model. The model ignores the quantum mechanic nature of spins (justified for large spins [136]), ignores possible anisotropy, and only includes pairwise interactions even though many-body effects may be present [103, 137]. Heisenberg MC is a step above mean-field estimates, but these shortcomings should be addressed in order to fully describe a magnetic system. Also, instead of using MC, magnetic dynamics could be studied via spin dynamics simulations [138].

In conclusion, two physical systems, diluted magnetic semiconductors and etched silicon surfaces, were simulated using multiscale methods. A major part of this work has been the construction of the applied Monte Carlo models, linking the atomistic calculations to the observed macroscopic phenomena. The developed models are system specific and contain several phenomenological aspects, showing the inherent difficulty in physical modeling: a simulation gives wrong results if it omits important details, yet it is inefficient if too many unnecessary details are incorporated. The models focus on describing effects caused by microscopic impurities and impurity clusters, and subsequently demonstrate how the formation of clusters has dramatic effects on the behavior of the studied systems on the macroscopic level.

References

[1] H. Raebiger, T. Hynninen, A. Ayuela, and J. von Boehm, Physica B **376-377**, 643 (2006).

[2] M. A. Gosálvez, Y. Xing, T. Hynninen, M. Uwaha, A. S. Foster, R. M. Nieminen, and K. Sato, J. Micromech. Microeng. **17**, S27 (2007).

[3] T. Hynninen and M. A. Gosálvez, J. Chem. Phys. **129**, 156101 (2008).

[4] H. Ohno, Science **281**, 951 (1998).

[5] S. A. Wolf, D. D. Awschalom, R. A. Buhrman, J. M. Daughton, S. von Molnár, M. L. Roukes, A. Y. Chtchelkanova, and D. M. Treger, Science **294**, 1488 (2001).

[6] S. Pearton, C. Abernathy, G. Thaler, R. Frazier, D. Norton, F. Ren, Y. Park, J. Zavada, I. Buyanova, W. Chen, and A. Hebard, J. Phys.: Condensed Matt. **16**, R209 (2004).

[7] T. Dietl and H. Ohno, Materials Today **9**, 18 (2006).

[8] T. Dietl, H. Ohno, F. Matsukura, J. Cibert, and D. Ferrand, Science **287**, 1019 (2000).

[9] H. Seidel, L. Csepregi, A. Heuberger, and H. Baumgärtel, J. Electrochem. Soc. **137**, 3612 .

[10] H. Seidel, L. Csepregi, A. Heuberger, and H. Baumgärtel, J. Electrochem. Soc. **137**, 3626 .

[11] N. Maluf and K. Williams, *An introduction to microelectromechanical system engineering*, 2nd ed. (Artech House, 2004).

[12] M. A. Gosálvez and H. Seidel, in *Part IV of Handbook of Silicon Based MEMS Materials and Technologies*, edited by V. K. Lindroos, M. Tilli, A. Lehto, and T. Motooka (William Andrew Publishing, Scheduled Dec. 2008), Chap. 23.

[13] D. Saya, K. Fukushima, H. Toshiyoshi, G. Hashiguchi, H. Fujita, and H. Kawakatsu, Sensors and Actuators A **95**, 281 (2002).

[14] J. W. Kwon and E. S. Kim, Sensors and Actuators A **97-98**, 729 (2002).

[15] H. J. G. E. Gardeniers, R. Luttge, E. J. W. Berenschot, M. J. de Boer, S. Y. Yeshurun, M. Hefetz, R. van't Oever, and A. van den Berg, J. Microelectromech. Syst. **12**, 855 (2003).

[16] G. Schröpfer, M. de Labachelerie, S. Ballandras, and P. Blind, J. Micromech. Microeng. **8**, 77 (1998).

[17] C. M. A. Ashruf, P. J. French, P. M. M. C. Bressers, P. M. Sarro, and J. J. Kelly, Sensors and Actuators A **66**, 284 (1998).

[18] M. A. Gosálvez, K. Sato, A. S. Foster, R. M. Nieminen, and H. Tanaka, J. Micromech. Microeng. **17**, S1 (2007).

[19] A. Mauger and C. Godart, Phys. Rep. **141**, 51 (1986).

[20] R. A. de Groot, F. M. Mueller, P. G. van Engen, and K. H. J. Buschow, Phys. Rev. Lett. **50**, 2024 (1983).

[21] H. Munekata, H. Ohno, S. von Molnar, A. Segmüller, L. L. Chang, and L. Esaki, Phys. Rev. Lett. **63**, 1849 (1989).

[22] T. Jungwirth, J. Sinova, J. Mašek, J. Kučera, and A. H. MacDonald, Rev. Mod. Phys. **78**, 809 (2006).

[23] C. Timm, J. Phys.: Condensed Matt. **15**, R1865 (2003).

[24] A. Kaminski and S. Das Sarma, Phys. Rev. Lett. **88**, 247202 (2002).

[25] H. Ohno, A. Shen, F. Matsukura, A. Oiwa, A. Endo, S. Katsumoto, and Y. Iye, Appl. Phys. Lett. **69**, 363 (1996).

[26] A. Shen, H. Ohno, F. Matsukura, Y. Sugawara, N. Akiba, T. Kuroiwa, A. Oiwa, A. Endo, S. Katsumoto, and Y. Iye, J. Crystal Growth **175-176**, 1069 (1997).

[27] F. Matsukura, A. Oiwa, A. Shen, Y. Sugawara, N. Akiba, T. Kuroiwa, H. Ohno, A. Endo, S. Katsumoto, and Y. Iye, Appl. Surf. Sci. **113-114**, 178 (1997).

[28] A. H. MacDonald, P. Schiffer, and N. Samarth, Nature Materials **4**, 195 (2005).

[29] F. Matsukura, H. Ohno, A. Shen, and Y. Sugawara, Phys. Rev. B **57**, R2037 (1998).

[30] K. W. Edmonds, K. Y. Wang, R. P. Campion, A. C. Neumann, N. R. S. Farley, B. L. Gallagher, and C. T. Foxon, Appl. Phys. Lett. **81**, 4991 (2002).

[31] K. W. Edmonds, P. Boguslawski, K. Y. Wang, R. P. Campion, S. N. Novikov, N. R. S. Farley, B. L. Gallagher, C. T. Foxon, M. Sawicki, T. Dietl, M. Buongiorno Nardelli, and J. Bernholc, Phys. Rev. Lett. **92**, 037201 (2004).

[32] K. Y. Wang, R. P. Campion, K. W. Edmonds, M. Sawicki, T. Dietl, C. T. Foxon, and B. L. Gallagher, AIP Conference Proceedings **772**, 333 (2005), arXiv:cond-mat/0411475.

[33] S. J. Potashnik, K. C. Ku, S. H. Chun, J. J. Berry, N. Samarth, and P. Schiffer, Appl. Phys. Lett. **79**, 1495 (2001).

[34] V. Stanciu, O. Wilhelmsson, U. Bexell, M. Adell, J. Sadowski, J. Kanski, P. Warnicke, and P. Svedlindh, Phys. Rev. B **72**, 125324 (2005).

[35] L. Kronik, M. Jain, and J. Chelikowsky, Phys. Rev. B **66**, 041203(R) (2002).

[36] A. Wolos, M. Palczewska, M. Zajac, J. Gosk, M. Kaminska, A. Twardowski, M. Bockowski, I. Grzegory, and S. Porowski, Phys. Rev. B **69**, 115210 (2004).

[37] B. Sanyal, O. Bengone, and S. Mirbt, Phys. Rev. B **68**, 205210 (2003).

[38] K. Sato, W. Schweika, P. H. Dederichs, and H. Katayama-Yoshida, Phys. Rev. B **70**, 201202(R) (2004).

[39] M. E. Overberg, C. R. Abernathy, S. J. Pearton, N. A. Theodoropoulou, K. T. McCarthy, and A. F. Hebard, Appl. Phys. Lett. **79**, 1312 (2001).

[40] M. L. Reed, N. A. El-Masry, H. H. Stadelmaier, M. K. Ritums, M. J. Reed, C. A. Parker, J. C. Roberts, and S. M. Bedair, Appl. Phys. Lett. **79**, 3473 (2001).

[41] S. Sonoda, S. Shimizu, T. Sasaki, Y. Yamamoto, and H. Hori, J. Cryst. Growth **237-239**, 1358 (2002).

[42] S. Dhar, O. Brandt, A. Trampert, L. Däweritz, K. J. Friedland, K. H. Ploog, J. Keller, B. Beschoten, and G. Güntherodt, Appl. Phys. Lett. **82**, 2077 (2003).

[43] R.Giraud, S. Kuroda, S. Marcet, E. Bellet-Amalric, X. Biquard, B. Barbara, D. Fruchart, D. Ferrand, J. Cibert, and H. Mariette, Europhys. Lett. **65**, 553 (2004).

[44] G. P. Das, B. K. Rao, and P. Jena, Phys. Rev. B **68**, 035207 (2003).

[45] B. K. Rao and P. Jena, Phys. Rev. Lett. **89**, 185504 (2002).

[46] L. M. Sandratskii, P. Bruno, and S. Mirbt, Phys. Rev. B **71**, 045210 (2005).

[47] X. Y. Cui, B. Delley, A. J. Freeman, and C. Stampfl, Phys. Rev. B **76**, 045201 (2007).

[48] K. Sato, H. Katayama-Yoshida, and P. Dederichs, Jpn. J. Appl. Phys. **44**, L948 (2005).

[49] K. Sato, T. Fukushima, and H. Katayama-Yoshida, J. Phys.: Condensed Matt. **19**, 365212 (2007).

[50] G. Martínez-Criado, A. Somogyi, S. Ramos, J. Campo, R. Tucoulou, M. Salome, J. Susini, M. Hermann, M. Eickhoff, and M. Stutzmann, Appl. Phys. Lett. **86**, 131927 (2005).

[51] G. Martínez-Criado, A. Somogyi, M. Hermann, M. Eickhoff, and M. Stutzmann, Jpn. J. Appl. Phys. **43**, L695 (2004).

[52] J. Rappich, H. J. Lewerenz, and H. Gerischer, J. Electrochem. Soc. **140**, L187 (1993).

[53] P. Allongue, Phys. Rev. Lett. **77**, 1986 (1996).

[54] M. A. Hines, Annu. Rev. Phys. Chem. **54**, 29 (2003).

[55] P. Allongue, V. Costa-Kieling, and H. Gerischer, J. Electrochem. Soc. **140**, 1009 (1993).

[56] P. Allongue, V. Kieling, and H. Gerischer, Electrochim. Acta **40**, 1353 (1995).

[57] Wet-chemical etching and cleaning of silicon, Virginia Semiconductor, Inc., 2003.

[58] S. P. Garcia, H. Bao, and M. A. Hines, Phys. Rev. Lett. **93**, 166102 (2004).

[59] H. Schröder, E. Obermeier, and A. Steckenborn, J. Micromech. Microeng. **9**, 139 (1999).

[60] W. Haiss, P. Raisch, L. Bitsch, R. J. Nichols, X. Xia, J. J. Kelly, and D. J. Schiffrin, J. Electroanal. Chem. **597**, 1 (2006).

[61] S. A. Campbell, K. Cooper, L. Dixon, R. Earwaker, S. N. Port, and D. J. Schiffrin, J. Micromech. Microeng. **5**, 209 (1995).

[62] H. Tanaka, Y. Abe, T. Yoneyama, J. Ishikawa, O. Takenaka, and K. Inoue, Sensors and Actuators A **82**, 270 (2000).

[63] H. Tanaka, D. Cheng, M. Shikida, and K. Sato, Sensors and Actuators A **128**, 125 (2006).

[64] M. Shikida, T. Masuda, D. Uchikawa, and K. Sato, Sensors and Actuators A **90**, 223 (2001).

[65] E. van Veenendaal, K. Sato, M. Shikida, and J. van Suchetelen, Sensors and Actuators A **93**, 219 (2001).

[66] S. P. Garcia, H. Bao, and M. A. Hines, J. Phys. Chem. B **108**, 6062 (2004).

[67] A. J. Nijdam, E. van Veenendaal, H. M. Cuppen, J. van Suchtelen, M. L. Reed, J. G. E. Gardeniers, W. J. P. van Enckevort, E. Vlieg, and M. Elwenspoek, J. Appl. Phys. **89**, 4113 (2001).

[68] E. van Veenendaal, K. Sato, M. Shikida, A. J. Nijdam, and J. van Suchtelen, Sensors and Actuators A **93**, 232 (2001).

[69] M. A. Gosálvez and R. M. Nieminen, New J. Phys. **5**, 100 (2003).

[70] *A primer in density functional theory*, edited by C. Fiolhais, F. Noguiera, and M. Marques (Springer, 2003).

[71] R. Parr and W. Yang, *Density Functional Theory of Atoms and Molecules* (Oxford University Press, 1989).

[72] P. Hohenberg and W. Kohn, Phys. Rev. **136**, B864 (1964).

[73] W. Kohn and L. J. Sham, Phys. Rev. **140**, A1133 (1965).

[74] O. Gunnarsson, B. I. Lundqvist, and J. W. Wilkins, Phys. Rev. B **10**, 1319 (1974).

[75] G. Kresse and J. Furthmüller, Phys. Rev. B **54**, 11169 (1996).

[76] J. Junquera, Ó. Paz, D. Sánchez-Portal, and E. Artacho, Phys. Rev. B **64**, 235111 (2001).

[77] J. M. Soler, E. Artacho, J. D. Gale, A. García, J. Junquera, P. Ordejón, and D. Sánchez-Portal, J. Phys.: Condensed Matt. **14**, 2745 (2002).

[78] J. P. Perdew, J. A. Chevary, S. H. Vosko, K. A. Jackson, M. R. Pederson, D. J. Singh, and C. Fiolhais, Phys. Rev. B **46**, 6671 (1992).

[79] J. P. Perdew, K. Burke, and M. Ernzerhof, Phys. Rev. Lett. **77**, 3865 (1996).

[80] A. D. Becke, Phys. Rev. A **38**, 3098 (1988).

[81] C. Lee, W. Yang, and R. G. Parr, Phys. Rev. B **37**, 785 (1988).

[82] J. P. Perdew, S. Kurth, A. Zupan, and P. Blaha, Phys. Rev. Lett. **82**, 2544 (1999).

[83] V. I. Anisimov, J. Zaanen, and O. K. Andersen, Phys. Rev. B **44**, 943 (1991).

[84] S. L. Dudarev, G. A. Botton, S. Y. Savrasov, C. J. Humphreys, and A. P. Sutton, Phys. Rev. B **57**, 1505 (1998).

[85] J. P. Perdew and A. Zunger, Phys. Rev. B **23**, 5048 (1981).

[86] A. D. Becke, J. Chem. Phys. **98**, 1372 (1993).

[87] J. P. Perdew, M. Ernzerhof, and K. Burke, J. Chem. Phys. **105**, 9982 (1996).

[88] S. F. Boys and F. Bernadi, Mol. Phys. **19**, 553 (1970).

[89] H. Monkhorst and J. Pack, Phys. Rev. B **13**, 5188 (1976).

[90] J. C. Phillips, Phys. Rev. **112**, 685 (1958).

[91] P. Blöchl, Phys. Rev. B **50**, 17953 (1994).

[92] P. Blöchl, C. J. Först, and J. Schimpl, Bull. Mater. Sci. **26**, 33 (2003).

[93] G. Kresse and D. Joubert, Phys. Rev. B **59**, 1758 (1999).

[94] N. Troullier and J. L. Martins, Phys. Rev. B **43**, 1991 (1991).

[95] H. Raebiger, A. Ayuela, J. von Boehm, and R. M. Nieminen, J. Magn. Magn. Mater. **290-291**, 1398 (2005).

[96] H. Raebiger, A. Ayuela, and J. von Boehm, Phys. Rev. B **72**, 014465 (2005).

[97] K. Binder and D. Heermann, *Monte Carlo simulation in statistical physics: an introduction*, *Solid state sciences*, 4th ed. (Springer, 2002).

[98] H. Raebiger, M. G. Ganchenkova, and J. von Boehm, Appl. Phys. Lett. **89**, 012505 (2006).

[99] N. Metropolis, A. W. Rosenbluth, M. N. Rosenbluth, A. H. Teller, and E. Teller, J. Chem. Phys. **21**, 1087 (1953).

[100] U. Wolff, Phys. Rev. Lett. **62**, 361 (1989).

[101] R. H. Swendsen and J.-S. Wang, Phys. Rev. Lett. **58**, 86 (1987).

[102] W. Heisenberg, Z. Phys. **49**, 619 (1928).

[103] M. van Schilfgaarde and O. N. Mryasov, Phys. Rev. B **63**, 233205 (2001).

[104] T. Hynninen, Master's thesis, Helsinki University of Technology, 2005.

[105] K. Binder, Phys. Rev. Lett. **47**, 693 (1981).

[106] A. P. J. Jensen, An Introduction To Monte Carlo Simulations Of Surface Reactions, arXiv:cond-mat/0303028v1, 2003.

[107] A. B. Bortz, M. H. Kalos, and J. L. Lebowitz, J. Comp. Phys. **17**, 10 (1975).

[108] J. L. Blue, I. Beichl, and F. Sullivan, Phys. Rev. E **51**, R867 (1995).

[109] M. A. Gosálvez, A. S. Foster, and R. M. Nieminen, Appl. Surf. Sci. **202**, 160 (2002).

[110] M. A. Gosálvez, Y. Xing, K. Sato, and R. M. Nieminen, J. Micromech. Microeng. **18**, 055029 (2008).

[111] Z. Zhou, Q. Huang, W. Li, and W. Deng, J. Micromech. Microeng. **17**, S38 (2007).

[112] M. A. Gosálvez, Y. Xing, and K. Sato, J. Microelectromech. Syst. **17**, 410 (2008).

[113] A. Bowyer, Computer Journal **24**, 162 (1981).

[114] D. F. Watson, Computer Journal **24**, 167 (1981).

[115] K. Hara, T. Tanii, and I. Ohdomari, Japanese Journal of Applied Physics **38**, 6860 (1999).

[116] M. G. Ganchenkova, V. A. Borodin, and R. M. Nieminen, Nucl. Inst. Meth. Phys. Res. B **228**, 218 (2005).

[117] Y. D. Park, A. T. Hanbicki, S. C. Erwin, C. S. Hellberg, J. M. Sullivan, J. E. Mattson, T. F. Ambrose, A. Wilson, G. Spanos, and B. T. Jonker, Science **295**, 651 (2002).

[118] S. Kirkpatrick, C. D. Gelatt Jr., and M. P. Vecchi, Science **220**, 671 (1983).

[119] M. Wierzbowska, D. Sánchez-Portal, and S. Sanvito, Phys. Rev. B **70**, 235209 (2004).

[120] J. Kudrnovský, I. Turek, V. Drchal, F. Máca, P. Weinberger, and P. Bruno, Phys. Rev. B **69**, 115208 (2004).

[121] P. Mahadevan, A. Zunger, and D. Das Sarma, Phys. Rev. Lett. **93**, 177201 (2004).

[122] L. M. Sandratskii and P. Bruno, Phys. Rev. B **66**, 134435 (2002).

[123] A. J. R. da Silva, A. Fazzio, R. R. dos Santos, and L. E. Oliveira, Phys. Rev. B **72**, 125208 (2005).

[124] P. Dev, Y. Xue, and P. Zhang, Phys. Rev. Lett. **100**, 117204 (2008).

[125] F. Filippone, G. Mattioli, and A. A. Bonapasta, J. Phys.: Condensed Matt. **20**, 125215 (2008).

[126] P. Larson and S. Satpathy, Phys. Rev. B **76**, 245205 (2007).

[127] J. L. Xu, M. van Schilfgaarde, and G. D. Samolyuk, Phys. Rev. Lett. **94**, 097201 (2005).

[128] N. Tandon, G. P. Das, and A. Kshirsagar, Phys. Rev. B **77**, 205206 (2008).

[129] T. Dietl, Phys. Rev. B **77**, 085208 (2008).

[130] D. Iuşan, B. Sanyal, and O. Eriksson, J. Appl. Phys. **101**, 09H101 (2007).

[131] H. Tanaka, D. Cheng, M. Shikida, and K. Sato, Sensors and Actuators A **134**, 465 (2007).

[132] E. D. Palik, O. J. Glembocki, I. Heard, Jr., P. S. Bruno, and L. Tenerz, J. Appl. Phys. **70**, 3291 (1991).

[133] C.-R. Yang, P.-Y. Chen, Y.-C. Chiou, and R.-T. Lee, Sensors and Actuators A **119**, 263 (2005).

[134] H. Raebiger, A. Ayuela, and R. M. Nieminen, J. Phys.: Condensed Matt. **16**, L457 (2004).

[135] M. H. Hakala, O. H. Pakarinen, and A. S. Foster, Phys. Rev. B **78**, 045418 (2008).

[136] C. Domb and M. Sykes, Phys. Rev. **128**, 168 (1962).

[137] I. P. R. Moreira, N. Suaud, N. Guihéry, J. P. Malrieu, R. Caballol, J. M. Bofill, and F. Illas, Phys. Rev. B **66**, 134430 (2002).

[138] V. P. Antropov, M. I. Katsnelson, M. van Schilfgaarde, and B. N. Harmon, Phys. Rev. Lett. **75**, 729 (1995).

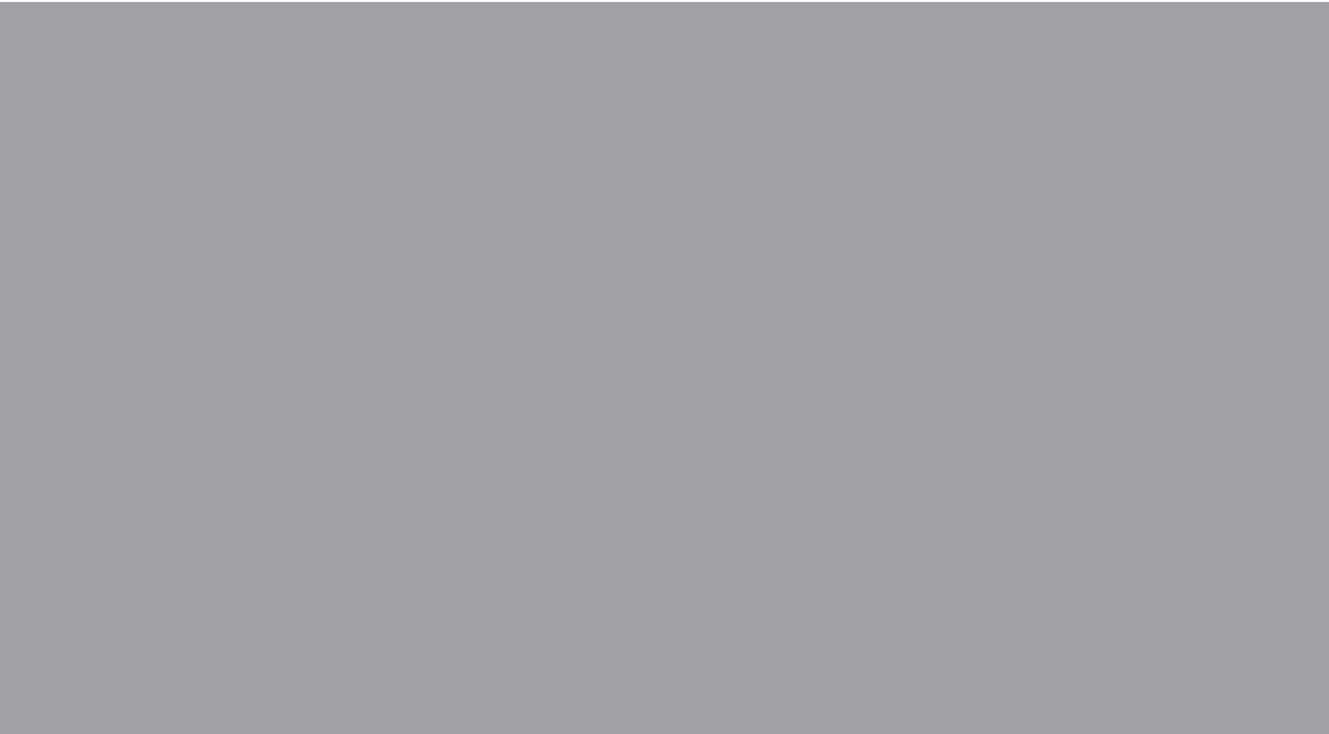

ISBN 978-951-22-9681-1
ISBN 978-951-22-9682-8 (PDF)
ISSN 1795-2239
ISSN 1795-4584 (PDF)